(2)

DARPA/ONR Grant #N00014-91-J-1976

Nineth Quarterly Progress Report
(covering the period of 08/01/93 - 10/31/93)

Project Title: Development of Ultra-Low Noise, High Performance III-V Quantum Well Infrared Photodetectors (QWIPs) for Focal Plane Array Staring Image Sensor Systems

Submitted to

Max N. Yoder

Office of Naval Research
Code 3140
800 North Quincy Street
Arlington, VA 22217-5000

Prepared by

Sheng S. Li
Professor

Dept. of Electrical Engineering
University of Florida
Gainesville, Florida 32611

Tel.(904)-392-4937
Fax(904)-392-8671
E-Mail: ShengLi@ENG.UFL.EDU

November 1, 1993

DARPA/ONR Grant #N00014-91-J-1976

Nineth Quarterly Progress Report
(covering the period of 08/01/93 - 10/31/93)

Project Title: Development of Ultra-Low Noise, High Performance III-V Quantum Well Infrared Photodetectors (QWIPs) for Focal Plane Array Staring Image Sensor Systems

Submitted to

Max N. Yoder

Office of Naval Research
Code 3140
800 North Quincy Street
Arlington, VA 22217-5000

Prepared by

Sheng S. Li
Professor

Dept. of Electrical Engineering
University of Florida
Gainesville, Florida 32611

Tel.(904)-392-4937
Fax(904)-392-8671
E-Mail: ShengLi@ENG.UFL.EDU

November 1, 1993

REPORT DOCUMENTATION PAGE

Form Approved
OMB No. 0704-0188

1. AGENCY USE ONLY (Leave blank)	2. REPORT DATE	3. REPORT TYPE AND DATES COVERED
	November 1, 93	Quarterly progress report: 8/1/93 - 10/31/93.

4. TITLE AND SUBTITLE
Development of Ultra-Low Noise, High Sensitivity Planar Metal Grating Coupled III-V Quantum Well Infrared Detectors for Focal Plane Array Staring IR Sensor Systems

5. FUNDING NUMBERS
ONR G-N00014-91-J-1976

6. AUTHOR(S)
Sheng S. Li, Professor

7. PERFORMING ORGANIZATION NAME(S) AND ADDRESS(ES)
University of Florida
Gainesville, FL 32611-6200

8. PERFORMING ORGANIZATION REPORT NUMBER
92122803

9. SPONSORING/MONITORING AGENCY NAME(S) AND ADDRESS(ES)
US Navy, Office of Naval Research
800 North Quincy Street, Code 1512B:SM
Arlington, VA 22217-5000

10. SPONSORING/MONITORING AGENCY REPORT NUMBER

11. SUPPLEMENTARY NOTES

12a. DISTRIBUTION/AVAILABILITY STATEMENT
Approved for public release, distribution unlimited.

12b. DISTRIBUTION CODE

13. ABSTRACT *(Maximum 200 words)*

During this reporting period (08-01-93 to 10-31-93) we have continued to make significant progress towards the program goals. We have made a major breakthrough in the development of a new normal incidence p-type strained-layer InGaAs/InAlAs QWIP grown on InP by MBE, which achieved an ultra-low dark current and very high detectivity at 8.1 um and 77 K. The detector is under background limited performance (BLIP) for T<100 K, which is the highest BLIP temperature ever reported for a QWIP. A dark current density of $7x10^{-8}$ A/cm^2 and BLIP detectivity of $5.9x10^{10}$ Jones were obtained for this QWIP at 77 K. Other tasks perrformed during this period include: (i) Design and fabrication of a new two-color stacked BTM and BTC QWIP for 3-5 and 8-12 um IR detection, (ii) design and growth of a normal incidence p-type strained -layer InGaAs/GaAs QWIP grown on GaAs by MBE, and (iii) theoretical and experimental studies of a two-dimensional (2- D) circular mesh grating coupler for GaAs QWIP for enhancing the coupling quantum efficiency and responsivity under normal incidence illumination. Detailed results and accomplishments are described in this report.

14. SUBJECT TERMS GaAs/GaAlAs Quantum well infrared photodetectors (QWIPs), p-type strained-layer InGaAs/InAlAs QWIP, intersubband absorption, dark current, responsivity, detectivity, 2-D circular mesh metal grating coupler.

15. NUMBER OF PAGES 40

16. PRICE CODE

17. SECURITY CLASSIFICATION OF REPORT	18. SECURITY CLASSIFICATION OF THIS PAGE	19. SECURITY CLASSIFICATION OF ABSTRACT	20. LIMITATION OF ABSTRACT
Unclassified.			Unlimited

9th Quarterly Progress Report (08/1/93 - 10/31/93)

Project Title: Development of Ultra-Low Dark Current, High Performance III-V Quantum Well Infrared Photodetectors (QWIPs) for Focal Plane Arrays Staring Imaging Sensor Systems.

Program Manager: Max N. Yoder, Office of Naval Research, Code 3140, Arlington, VA.

Principal Investigator: Sheng S. Li, Professor, University of Florida, Gainesville, FL.

Project Objectives:

1. To develop ultra-low dark current and high detectivity planar metal grating coupled bound-to-miniband (BTM) III-V quantum well infrared photodetectors (QWIPs) for 8 to 12 μm focal plane arrays (FPAs) staring IR sensor systems.

2. To develop novel III-V QWIPs with single, multicolor, broad and narrow band spectral responses in the 8 to 14μm wavelength range. The material systems to be studied include n-type GaAs/AlGaAs and AlAs/AlGaAs grown on GaAs substrates, n-type InAlAs/InGaAs and p-type strained-layer InAlAs/InGaAs grown on InP substrates.

3. To conduct theoretical and experimental studies of the planar 2-D metal grating coupled structures for normal incidence illumination on QWIPs. Different metal grating coupled structures using 2-D square mesh and dot metal gratings will be studied in order to achieve high coupling quantum efficiency under normal frontside or backside illuminations.

4. To perform theoretical and experimental studies of dark current, photocurrent, noise figures optical absorption, spectral responsivity and detectivity for different types of QWIPs developed under this program.

I. Introduction

During this reporting period (08-01-93 to 10-31-93) we have continued to make excellent progress towards the program goals. We have designed, fabricated, and characterized a new normal incidence p-type strained-layer (PSL) InGaAs/InAlAs QWIP formed on the InP substrate, which simultaneously achieved the **lowest dark current and highest detectivity** ever reported for a QWIP operating at $\lambda_p = 8.1$ μm and T = 77 K. The device dark current for this QWIP operating at 77 K is about two orders of magnitude smaller than the 300 K background photocurrent, and was under**BLIP** condition for T$\leq$ 100 K. *Specific tasks performed during this period include: (i)* design, growth, fabrication, and characterization of a novel ultra-low dark current normal incidence p-type strained-layer InGaAs/InAlAs QWIP grown on a semi-insulating InP substrate by the MBE technique, (ii) design, growth, and fabrication of a new multi-color enhanced bound-to-continuum band (EBTC) and bound-to-miniband (BTM) transition GaAs/GaAlAs QWIPs grown on GaAs substrate by MBE technique, (iii) design and growth of a normal incident p-type strained layer InGaAs/GaAs QWIP on GaAs substrate, (iv) design 2-D circular mesh metal grating coupler structures for a GaAs QWIP to enhance the coupling quantum efficiency and to improve the responsivity and detectivity of this QWIP, (v) perform theoretical and experimental studies of the 2-D circular mesh grating coupled GaAs/AlGaAs QWIP for improving coupling quantum efficiency and responsivity. A list of accomplishments and publications are given in Section II. The technical results are presented in Section III.

II. Research Accomplishments and Publications

Research accomplishments and publications supported by this ARPA/ONR grant are summarized as follows:

2.1 Research Accomplishments:

1. A new normal incidence p-type strained (PSL) InGaAs/InAlAs QWIP with peak response wavelength at $\lambda_p = 8.1$ μm and operating under background limited performance (BLIP) condition at 77 K has been developed for the first time. This detector is under BLIP for T $\leq$ 100 K, which is the highest BLIP temperature ever reported for a QWIP.The BLIP detectivity for this QWIP at peak wavelength $\lambda_p = 8.1$ μm was found to be 5.9×10^{10} $cm - Hz^{1/2}/W$, at $V_b = 2$ V and T = 77 K. The extremely low dark current density (7×10^{-8} A/cm^2) observed in this QWIP at 77 K offers an excellent opportunity to fabricate high performance focal plane

arrays using PSL-QWIPs for 77 K operation. Detailed results for this QWIP are depicted in Section 3.1.

2. Design and growth of a new p-type strained-layer InGaAs/GaAs QWIP on SI GaAs substrate have been carried out. Device fabrication and characterization of this new QWIP will be performed during the next reporting period.

3. Theoretical and experimental studies of a 2-D circular mesh metal grating coupler formed on a GaAs QWIP have been carried out. Detailed results are discussed in Section 3.2.

4. Since the beginning of this project, one Ph.D. and three M.S. students have completed their degree working on the QWIP project sponsored by the ARPA/ONR grant. Two more Ph.D. students are in their final stage of research and are expected to graduate by Summer term, 1994. An AASERT sponsored Ph.D. student has started this summer working on the new high performance p-type strained-layer InGaAs/InAlAs QWIPs for focal plane arrays applications.

5. Dr.Li presented an **invited talk** on the Grating Coupled and Normal Incidence III-V QWIPs at the ***NATO Advanced Research Workshop on Intersubband Transition Physics and Devices***, Whistler, Canada, Sept.7-10, 1993.

6. Dr.Li presented an **invited talk** on Grating Coupled III-V QWIPs for Mid- and Long-Wavelength Infrared (LWIR) Detection,at the ***First Int. Symposium on Long Wavlength Infrared Detectors and Arrays***, Electrochemical Society Meeting, New Orlean, October 10-13, 1993.

2.2. Refereed Journal Papers:

1. L. S. Yu and**S. S. Li**,"A Low Dark Current, High Detectivity Grating Coupled AlGaAs/GaAs Mulitple Quantum Well IR Detector Using Bound-to-Miniband Transition for 10 μm Detection,"Appl. Phys. Letts., 59 (11), p.1332, Sept.9, 1991.

2. L. S. Yu,**S. S. Li**, and Pin Ho "Largely Enhanced Bound-to-Miniband Absorption in an InGaAs Multiple Quantum Well with a Short-Period Superlattice InAlAs/InGaAs Barrier " Applied Phys. Letts., 59 (21), p.2712, Nov. 18, 1991.

3. L. S. Yu, Y. H. Wang,**S. S. Li** and Pin Ho,"A Low Dark Current Step-Bound-to-Miniband Transition InGaAs/GaAs/AlGaAs Multiquantum Well Infrared Detector," Appl. Phys. Letts., 60(8), p.992, Feb.24, 1992.

4. L. S. Yu,**S. S. Li**,and P. Ho,"A Normal Incident Type-II Quantum Well Infrared Detector Using an Indirect AlAs/$Al_{0.5}Ga_{0.5}As$ System Grown on [110] GaAs,"Electronics Letts., 28(15) p.1468, July,16, 1992.

5. L. S. Yu,**S. S. Li**, Y. H. Wang, and Y. C. Kao,"A Study of Coupling Efficiency versus Grating Periodicity in A Normal Incident Grating-Coupled GaAs/AlGaAs Quantum Well Infrared Detector," J. Appl. Phys., 72(6), pp.2105, Sept. 15, 1992.

6. Y. H. Wang, S, S. Li, and P. Ho,"A Photovoltaic and Photoconductive Dual Mode Operation GaAs/AlGaAs Quantum Well Infrared Detector for Two Band Detection," Appl.Phys. Lett., 62(1), pp.93-95, Jan. 4 1993.

7. Y. H. Wang,**S. S. Li**, and P. Ho,"A Voltage-Tunable Dual Mode Operation InAlAs/InGaAs Bound-to-Miniband Transition QWIP for Narrow and Broad Band Detection at 10 μm," Appl. Phys. Lett., 62(6), pp.621-624, Feb. 8 , 1993.

8. P. Ho, P. A. Martin, L. S. Yu, and**S. S. Li**,"Growth of GaAs and AlGaAs on Misoriented (110) GaAs and a Normal Incidnece Type-II Quantum Well Infrared Detector," J. Vacuum Science and Technology B,11(3), pp.935-944, May/June, 1993.

9. **S. S. Li**, M. Y. Chuang and L. S. Yu,"Current Conduction Mechanisms in Bound-to-Miniband Transition III-V Quantum Well Infrared Photodetectors," *J. Semiconductor Science and Technology*, vol.8, pp.406-411, 1993.

10. Y. H. Wang,**S. S. Li**, P. Ho, and M. O. Manasreh, "A Normal Incidence Type-II Quantum Well Infrared Photodetector Using An Indirect AlAs/AlGaAs System Grown on [110] GaAs for the Mid- and Long-Wavelength Multicolor Detection," J. Appl. Phys., vol.74(2), pp.1382-87, July 15, 1993.

11. Y. C. Wang and**S. S. Li**,"A Numerical Analysis of Double Periodic Reflection Metal Grating Coupler for Multiquantum Well Infrared Photodetectors," J. Appl.Phys.,vol.74(4), pp.2192-96, August 15, 1993.

12. Y. C. Wang and**S. S. Li**," Design of A Two-Dimensional Square Mesh Metal Grating Coupler for GaAs/AlGaAs Quantum Well Infrared Photodetectors," J. Appl.Phys., accepted, Jan.1 issue,1994.

13. Y. H. Wang,**S. S. Li**, J. Chu, and P. Ho, "An Ultra-low Dark Current Normal Incidence P-type Strained Layer InGaAs/InAlAs QWIP with Background Limited Performance at 77 K," Appl. Phys. Lett., accepted, November, 1993.

2.3. Workshop and Conference Presentations

1. L. S. Yu, **S. S. Li**, and Pin Ho, " Largely Enhanced Intra-subband Absorption in a Wide InAlAS/InGaAs Quantum Well with a Short-Period Superlattice Barrier Structure,' presented at the ***SPIE's Symposium on Quantum Wells and Superlattices***, Somerset, NJ, 23-27 March,1992. Paper published in the SPIE Conference Proceeding.

2. **S. S. Li**and L. S. Yu, "Grating Coupled Bound-to-Miniband Transition III-V Quantum Well Infrared Detectors," **Invited Talk**, presented at ***the Innovative Long Wavelength Infrared Photodetector Workshop***, Jet Propulsion Lab., Pasadena, CA, April 7-9, 1992.

3. L. S. Yu and **S. S. Li**,"A Normal Incident Type-II Quantum Well Infrared Detector Using an Indirect AlAs/$Al_{0.5}Ga_{0.5}As$ System Grown on [110] GaAs, presented at ***the Innovative Long Wavelength Infrared Photodetector Workshop***, Jet Propulsion Lab., Pasadena, CA, April 7-9, 1992.

4. L. S. Yu, **S. S. Li**, Y. H. Wang, and P. Ho," Grating Coupled III-V Quantum Well Infrared Detectors Using Bound-to-Miniband Transition," presented at ***the SPIE Conference on Infrared Detectors and Focal Plane Arrays at OE/Aerospace Sensing 92***," Orlando, FL, April 20-24, 1992. Full paper published in the SPIE conference proceeding.

5. **S. S. Li**,"Grating Coupled Bound-to-Miniband Transition III-V Multiquantum Well Infrared Photodetectors," presented at the DARPA IR Detector Workshop, Washington D.C., June 12, 1992.

6. **S. S. Li**, M. Y. Chuang and L. S. Yu,"Current Conduction Mechanisms in Bound-to-Miniband Transition III-V Quantum Well Infrared Photodetectors," presented at the ***International Conference on Narrow Gap Semiconductors***, University of Southampton, Southampton, UK, July 19-23, 1992.

7. P. Ho, P. A. Martin, L. S. Yu, and **S. S. Li**,"Growth of GaAs and AlGaAs on Misoriented (110) GaAs and a Normal Incidnece Type-II Quantum Well Infrared Detector," presented at the ***12th North American Conference on Molecular Beam Epitaxy,***" Oct.12-14, 1992.

8. **S. S. Li**,"Novel Grating Coupled Miniband Transport III-V Multiquantum Well Infrared Photodetectors for Focal Plane Array Applications," presented at the DARPA IR Detector Workshop, Washington D.C., Dec 11, 1992.

9. **S. S. Li**, Y. H. Wang, M. Y. Chuang, P. Ho,"Photoconductive and Photovoltaic Dual-Mode Operation III-V Quantum Well Infrared Photodetectors for 2 - 14 μm Detection," presented at the Materials Research Society (MRS), Symposium C2 on **Infrared Detectors**, San Francisco, April 12-16, 1993.

10. D. Wang, Y. H. Wang, G. Bosman and **S. S. Li**,"Noise Characterization of Novel Quantum Well Infrared Photodetectors," **Invited Talk** presented at the ***12th Int. Conf. on Noise in Physical Systems and 1/f Fluctuations - The High Technologies Conference***, St. Louis, MO, August 16-20, 1993.

11. **S. S. Li**,"Some Novel High Performance III-V Quantum Well Infrared Photodetectors for Focal Plane Array Image Sensor Applications," **Invited Talk** presented at ***the NATO Advanced Research Workshop on Intersubband Transition Physics and Devices***, Whistler, Canada, September 7 - 10, 1993.

12. **S. S. Li**,"Grating Coupled III-V Quantum Well Infrared Photodetectors for Mid-Wavelength and Long-Wavelength Infrared Detection," **Invited Talk** presented at ***the First International Symposium on Long Wavelength Infrared Photodetectors*** in conjunction with the Fall Electrochemical Society (ECS) Meeting in New Orlean, LA, October 10 -15, 1993.

13. **S. S. Li**, Y. H. Wang, J. Chu, and P. Ho,"A Normal Incidence P-Type Strained-Layer InGaAs/InAlAs Quantum Well Infrared Photodetector with Background Limited Performance at 77 K," 1994 ***SPIE Conference on Infrared Detectors and Focal Plane Arrays III***, Orlando, FL, April 4-8, 1994.

2.4 Interactions with Government and Industrial Laboratories

1. Continued to collaborate with Dr. Pin Ho of General Electric Co.,in Syracuse, NY, on the growth of III-V QWIP's structures by using the MBE technique.

2. Contiuned to interact and exchange technical information on QWIP results with Dr. M. Tidrow of U.S. Army Electronics Tech. & Devices Laboratory, EPSD, Fort Monmouth, NJ.

3. Dr. Li was invited to give a seminar at the Electronics Technology Laboratory, WPAFB, Ohio, on ***The bound-to-miniband transition III-V QWIPs*** on August 21, 92, and discussed with Dr.Omar Manasreh and his colleagues in the Electronics Technology Laboratory at the WPAFB. Dr. Manasreh had performed optical absorption measurements on Dr. Li's QWIP samples, while Dr. Li has fabricated and characterized some QWIP samples provided by Dr. Manasreh. Dr. Li is currently writing a book chapter on grating coupled miniband transport QWIPs for a new book on ***Long Wavelength Quantum Well Infrared Photodetectors*** edited by Dr. Manasreh and to be published by Artech House in 1994.

4. Dr. Li was invited by the American Engineering Education Association (AEEA) to serve on a review panel for Naval Postdoctoral Fellowship program in Washington D.C. August 7, 92, to review a dozen of proposals submitted by various applicants.

5. Mr. Tom Briere of InfraMetrics has contacted Dr. Li, expressing his interest in using our QWIPs in the infrared imaging sensor applications. Dr. Li has sent a copy of his most recent ARPA quarterly progress report to Mr. Briere. Dr. Li will keep in touch with InfraMetrics on our new development in QWIP arrays.

6. Dr. Li has collaborated with Drs. Bill Beck and John Little of Martin Marietta Lab. (MML), in Baltimore, Maryland on QWIP research. Dr. Li has sent the normal incidence PSL-InGaAs/InAlAs QWIP sample to Dr. Beck for evaluation and for possible fabrication of focal plane arrays at MML.

7. Drs.Jan Andersson and Len Lundqvist (both working on grating coupled QWIP arrays) visited Dr. LI's Lab. on October 15, 1993, and presented a seminar on grating design for GaAs QWIPs at our Department.

8. Dr. Li has been invited by Electrochemcial Society (ECS) to co-organize the ***2nd. International Symposium on 2-20 μm Wavelength Infrared Detectors and Arrays: Physics and Applications*** to be held in Miami Beach, FL., October10-15, 1994.

9. The p-type strained-layer InGaAs/InAlAs QWIP developed recently in our Lab. has received considerable interest in QWIP community. We have received many requests from various industry, university, and government Labs. for the preprints of the PSL-QWIP paper presented at NATO Workshop and the First International Symposium on Long Wavelength Infrared Detectors and Arrays-ECS 93'.

III. Technical Results

3.1 A Normal Incidence, P-type Strained-Layer $In_{0.3}Ga_{0.7}As/In_{0.52}Al_{0.48}As$ Quantum Well Infrared Photodetector with Background Limited Performance at $\lambda_p = 8.1$ μm and T $\leq$ 100 K

Summary: An ultra-low dark current normal incidence p-type strained-layer $In_{0.3}Ga_{0.7}As/In_{0.52}Al_{0.48}As$ quantum well infrared photodetector (PSL-QWIP) grown on semi-insulating (100) InP substrate by MBE technique has been demonstrated for the first time. This PSL-QWIP shows a background limited performance (BLIP) for $T \leq 100$ K, which is the highest BLIP temperature ever reported for the QWIPs. Due to a 1.5 % lattice mismatch between the substrate and the quantum well, a biaxial tensile strain is created in the quantum well, which results in the inversion of the light-hole and heavy-hole ground state inside the quantum well. Since the light-hole state with large in-plane density of states becomes the ground state for the free holes with small effective mass, a large enhancement of the valence intersubband absorption occurs in this QWIP. The dark current density and the BLIP detectivity D^*_{BLIP} for this PSL-QWIP were found to be 7×10^{-8} A/cm^2 and 5.9×10^{10} $cm - \sqrt{Hz}/W$, respectively, at $\lambda_p = 8.1$ μm, $V_b = -2V$, and T = 77 K.

3.1.1 Introduction

Quantum well infrared photodetectors using n-type GaAs/AlGaAs and InGaAs/InAlAs systems for 8-14 μm IR detection have been extensively studied in recent years[1-12]. With low electron effective mass and high electron mobility, the n-type GaAs and InGaAs QWIPs offer excellent IR detection properties. However, the quantum mechanical selection rule for the intersubband transition requires that the radiation electric field has a component perpendicular to the quantum well plane (i.e., z-direction) in order to induce intersubband absorption in the quantum wells. As a result, for focal plane array (FPA) applications, the use of planar metal or dielectric grating structures for coupling IR radiation into the quantum well[3-5] becomes necessary to allow normal incidence illumination in the n-type QWIPs.

P-type QWIPs using valence intersubband transitions have been demonstrated recently in the lattice-matched GaAs/AlGaAs and InGaAs/InAlAs material systems[6-8]. Due to a mixing between the light-hole and heavy-hole states, normal incident illumination is allowed for the intersuband transition in p-type QWIPs. In general, the intersubband transitions under normal incident radiation in p-type quantum well are induced by the linear combination of p-like valence-band Bloch

states which provides a nonzero coupling between this component and the normal radiation field. The strong mixing between the light-hole and the heavy-hole states greatly enhances the normal incidence intersubband absorption. However, in the lattice-matched p-type QWIPs, the intersubband transition occurs between the heavy-hole ground state and the upper excited states. Due to the relatively large heavy-hole effective mass when compared to electron effective mass, a relative weak absorption and a similarly low responsivity are predicted for the unstrained p-type QWIPs in the IR wavelength range. If a biaxial tensile strain is intentionally introduced between the quantum well and the barrier layers, the effect of tensile strain can cause the inversion of heavy-hole state and light-hole ground state in the quantum well[13-14]. This in turn will cause the intersubband transition from the populated light-hole ground state to the upper energy band states. Since the light-hole has a large in-plane density of states and a small effective mass (comparable to the electron effective mass), the optical absorption and the responsivity of a PSL-QWIP can be greatly enhanced by using this new approach[14].

3.1.2. Theoretical Considerations

If a biaxial strain is intentionally introduced in the quantum well of a p-type $In_{0.3}Ga_{0.7}As/In_{0.52}Al_{0.48}As$ quantum well structure, the pseudomorphic or coherent heterointerfaces can be grown if the layer thickness is within a critical thickness. The strained-layers have the same effective in-plane lattice constant, $a_{||}$ (i.e., $a_{x,y}$), and can store the excess energy due to the elastic strain within the layers. The in-plane lattice constant, $a_{||}$, can be expressed by[9]

$$a_{||} = a_1 \left[1 + \delta_o / \left(1 + \frac{\xi_1 L_1}{\xi_2 L_2} \right) \right], \tag{1}$$

where $a_{1,2}$ and $L_{1,2}$ are the individual layer lattice constants and thicknesses, respectively, and $\xi_{1,2}$ are the shear moduli as described by $\xi = (C_{11} + C_{12} - 2C_{12}^2/C_{11})$, where the C_{ij}s are elastic constants for the strained material and can be found in reference (10). δ_o is the lattice mismatch between layers and is defined as $\delta_o = (a_2 - a_1)/a_1$, where a_2 and a_1 are the lattice constants of the strained well and the substrate (or barrier) respectively. If the QWIP structure is grown along the [100] direction and the strained-layer is within the critical thickness, L_c, then the components of the strain tensor [e] are simplified to the expressions below.

$$e_{xx} = e_{yy} = e_{||} \tag{2}$$

$$e_{zz} = -e_{||} \left(\frac{2C_{12}}{C_{11}} \right) \tag{3}$$

$$e_{xy} = e_{yz} = e_{zx} = 0 \tag{4}$$

In addition to altering the physical parameters of the QWIP, lattice strain can also induce energy band shifts, which can be used to alter the absorption characteristics of the QWIP. The strain induced energy band shifts for the conduction band, the heavy hole subband, and light hole subband can be approximated as follows.

$$\Delta E_c = 2c_1 \frac{C_{11} - C_{12}}{C_{11}} \delta_o \quad (5)$$

$$\Delta E_{hh} = b \frac{C_{11} + C_{12}}{C_{11}} \delta_o \quad (6)$$

$$\Delta E_{lh} = -\Delta E_{hh} + \frac{(\Delta E_{hh})^2}{2\Delta_o} \quad (7)$$

where c_1 is the combined hydrostatic deformation potential which characterizes the splitting of the Γ_8 valence band under strain and b is the shear deformation potential and Δ_o is the spin orbit split-off[10]. The total hydrostatic deformation potential ($c_1 + V_v$), where V_v is the valence band deformation potential, is given by[11]

$$c_1 + V_v = -\frac{1}{3}(C_{11} + 2C_{12}) \frac{dE_g^o}{dP}, \quad (8)$$

where dE_g^o/dP is the unstrained energy bandgap change with respect to the unit pressure.

The effect of strain on the energy band structure results in the splitting of the heavy- hole and light- hole bands at the valence band zone center[12] (i.e., the in-plane wavevector $k_{||} = 0$), which is degenerate in the unstrained case. When the tensile strain is applied between the quantum well and barrier layers[13–15] along the superlattice growth z-direction, the strain can push the light- hole levels upwards and pull the heavy- hole levels downwards. Therefore, we can expect that the inversion of the heavy- hole ground state and light- hole states in the quantum well at a certain lattice strain and quantum well thickness. This phenomena will in turn cause the intersubband transitions in a p-QWIP structure to be from the populated light-hole ground state to the upper energy band states. Since the light-hole has a small effective mass, the optical absorption and photon responsivity in p-type QWIPs can be greatly enhanced by the induced tensile strain in the quantum well. In fact, the calculated absorption coefficients by Xie et al.[15] for the $In_{0.3}Ga_{0.7}As/In_{0.52}Al_{0.48}As$ system with a 60 $\AA$ well width were found to be 5,000 and 8,500 cm^{-1} at λ_p = 8, 12 μm, respectively.

To calculate the locations of the energy subbands, we can use the transfer matrix method (TMM)[14,16], based on the eight-band $\mathbf{k \cdot p}$ model. This model is represented by the Luttinger-Kohn Hamiltonian[17,18], H_t, which describes the unstrained semiconductor.

$$H_t = H + V(z) \quad (9)$$

where

$$H = \begin{bmatrix} H_{11} & H_{12} & H_{13} & H_{14} \\ H_{21} & H_{22} & H_{23} & H_{24} \\ H_{31} & H_{32} & H_{33} & H_{34} \\ H_{41} & H_{42} & H_{43} & H_{44} \end{bmatrix} \tag{10}$$

with:

$$H_{11} = \frac{\gamma_1+\gamma_2}{2}(k_x^2 + k_y^2) + \frac{\gamma_1-\gamma_2}{2}k_z^2$$

$$H_{22} = \frac{\gamma_1-\gamma_2}{2}(k_x^2 + K_y^2) + \frac{\gamma_1+\gamma_2}{2}k_z^2$$

$$H_{12} = i\sqrt{3}\gamma_3(k_x - ik_y)k_z$$

$$H_{13} = \frac{\gamma_2\sqrt{3}}{2}(k_x^2 - k_y^2) - i\sqrt{3}\gamma_3 k_x k_y$$

$$H_{21} = H_{12'}^* \qquad H_{13} = H_{31'}^* \qquad H_{24} = H_{13}$$

$$H_{34} = H_{12'} \qquad H_{42}^* = H_{13'}^* \qquad H_{43} = H_{12}^*$$

$$H_{14} = H_{23} = H_{32} = H_{41} = 0$$

and V(z) is a step function which vanishes inside the well layers and equals V_o in the barrier layers. The effect of strain is included by adding the Pikus-Bir Hamiltonian[19], H_s, to the general Luttinger-Kohn Hamiltonian. As shown below, the strain Hamiltonian for the well material is a diagonal matrix.

$$H_s = \begin{bmatrix} -\Delta E_c - \Delta E_{hh} & 0 & 0 & 0 \\ 0 & -\Delta E_c + \Delta E_{hh} & 0 & 0 \\ 0 & 0 & -\Delta E_c + \Delta E_{hh} & 0 \\ 0 & 0 & 0 & \Delta E_c + \Delta E_{hh} \end{bmatrix} \tag{11}$$

Using the aforementioned techniques, we can numerically calculate the energy of the zone-center valence subband levels as a function of well width for any material systems under tensile or compressional strain and also determine the change in the valence subband structures. Figure 3.1.2 shows the calculate energy band diagrams at the valence band zone-center for the p-type InGaAs/InAlAs QWIP as a function of well thickness for the cases (a) without and (b) with biaxial tensile strain in the quantum well.

Since the heavy-hole and light- hole valence subbands are non-degenerate after the introduction of strain into the QWIP structure, a simpler method can be used to determine the energies of the subbands. By using the parabolic band approximation near the valence band zone-center, and the energy band shifts for the conduction band minimum, heavy-hole subband maximum, and light-hole

subband maximum; we can utilize the simpler two-band Hamiltonian for electrons just by finding the effective mass of the carriers (i.e., heavy hole effective mass and light hole effective mass) and the barrier heights for each carrier type. Although this does not simultaneously determine the energy levels of both carriers, it does allow accurate predictions of the energy subbands. When compared to the direct calculation of the energy subbands, the two-band approximation yields accurate results when compared to the direct calculation results[14,19] (see Fig.3.1.1). One limitation of the TMM is that this method cannot calculate the energy levels of the allowed energy subbands in the continuum. In order to determine the transition energy from the ground state to the continuum state, we used the Kronig-Penney approximation to determine the locations of the allowed energy bands in the continuum.

As can be easily seen in Fig.3.1.2, the influence of strain on the relative positions of the heavy-hole (HH) and light- hole (LH) subbands is apparent. When a biaxial internal tension is applied to the well material (in this case $Ga_{0.7}In_{0.3}As$ on an InP substrate with the barrier layers consisting of lattice matched $Al_{0.48}In_{0.52}As$), the strain pulls the LH subbands up with respect to the HH subbands for a given well thickness. While quantum confinement effects tend to push the LH subbands down with respect to the HH subbands. As the well width is increased above a certain value, the strain effect can overcome the quantum confinement effect and therefore induce the inversion of the heavy- hole and light- hole subbands at the ground state.

Although our band calculations can be used to determine the positions of the subbands in the quantum wells, and therefore determine the peak absorption wavelengths of the QWIP, many other factors must be taken into account to produce a successful detector. In general, for a good detector, the responsivity must be high, while the noise current must be low. The responsivity, R, for a photodetector can be expressed as[20]

$$R = \frac{q\lambda\eta p}{hc} G, \tag{12}$$

where q is the electronic charge, λ is the wavelength of the photon, h is Planck's constant, c is the speed of light, p is the tunneling probability out of the quantum well, η is the quantum efficiency and the photoconductive gain is G. The quantum efficiency and photoconductive gain can be described by[20]

$$\eta = A\left[1 - exp\left(-B\alpha l_{qw}\right)\right] \tag{13}$$

$$G = \frac{L}{t_c} \tag{14}$$

where A is a constant that is dependent on polarization, α is the absorption coefficient of the quantum well, l_{qw} is the total width of all quantum well regions, L is the mean free path of the carrier, and t_c is the total width of all quantum well and barrier regions. B is a constant dependent on the number of passes IR radiation makes through the photodetector. For n-type QWIPs A=0.5 while for p-type QWIPs A=1. The mean free path of the carrier may be expressed as[20]

$$L = \tau T_{qw} \mu_{eff} E, \tag{15}$$

where τ is the well recapture lifetime of the carrier, T_{qw} is the transmission coefficient over the quantum well, μ_{eff} is the effective mobility of the carrier, and E is the electric field. The effective mobility for a two-band transport model is shown to be[20]

$$\mu_{eff} = \frac{\Delta p_{lh} \mu_{lh} + \Delta p_{hh} \mu_{hh}}{\Delta p_{lh} + \Delta p_{hh}}, \tag{16}$$

where Δp_{hh} and Δp_{lh} are the concentrations of optically induced heavy- and light- hole carriers, respectively, and μ_{hh} and μ_{lh} are the respective heavy- and light- hole mobilities. When only the ground state is completely occupied, either Δp_{lh} or Δp_{hh} is negligible compared to the other states so that we may estimate μ_{eff} as the in-plane effective mass of the ground state carriers.

Another important parameter to be considered in the QWIP design is the dark current density (j_{dark}), which can be expressed using the Richardson-Dushman equation[15] as

$$j_{dark} \propto T^2 m^* exp\left(\frac{-\Delta E}{kT}\right), \tag{17}$$

where m^* is the effective mass, ΔE is the difference in energy between the barrier height and the quantum confined state in the well, k is the Boltzmann constant, and T is the temperature.

The noise in the QWIPs is mainly due to the random fluctuations of thermally excited carriers. The noise can be expressed as[6]

$$i_{noise} = \sqrt{4 A_d q G \Delta f j_{dark}}, \tag{18}$$

where A_d is the detector area, and Δf id the bandwidth. Finally, a figure of merit measurement used to compare QWIP's perfromance is the detectivity, D^*, which is given by[20]

$$D^* = \sqrt{A_d \Delta f} \frac{R}{i_{noise}}. \tag{19}$$

3.1.3. Results and Discussion

In this section, we discuss the fabrication of an ultra-low dark current, normal incidence p-type strained-layer (PSL) $In_{0.3}Ga_{0.7}As/In_{0.52}Al_{0.48}As$ QWIP using the intersubband transition from the

ground light-hole state (E_{LH1}) to the heavy-hole continuum states (E_{HH3}) for 8.1 μm detection, as shown in Fig.3.1.1. The PSL-QWIP structure was grown on the (100) semi-insulating (SI) InP substrate using MBE technique. The PSL-QWIP structure consists of 20 periods of 4-nm Be-doped $In_{0.3}Ga_{0.7}As$ quantum well with a dopant density of 1×10^{18} cm^{-3} separated by 45-nm $In_{0.52}Al_{0.48}As$ undoped barrier layer. A 0.3 μm cap layer and a 1μm buffer layer of Be-doped $In_{0.53}Ga_{0.47}As$ with a dopant density of 2×10^{18} cm^{-3} were grown for the top and bottom ohmic contacts. The contact and barrier layers are lattice-matched to the InP substrate, whereas the quantum well layers are in biaxial tension with a lattice mismatch of about 1.5% between the well and the barrier layers. In order to measure the spectral responsivity and the dark current of this PSL-QWIP, a 200×200 μm^2 mesa structure was formed by using the chemical etching process. The Au/Zn alloy was thermally evaporated onto the QWIP mesas with a film thickness of 1500 $\AA$, followed by annealing at 480 °C for 5 minutes to obtain stable and low contact resistance.

Figure 3.1.3 shows the measured dark current at T = 77, 90, 100, and 110 K, and the 300 K background photocurrent density for this PSL-QWIP. The device shows asymmetric dark current characteristic under positive and negative bias, which is attributed to the band bending due to dopant migration effect[21] as shown in Fig.3.1.1. The dark current density was found to be equal to 7×10^{-8} A/cm^2 at V_b = 2 V and T = 77 K. In fact, this PSL-QWIP is under background limited performance (BLIP) with field of view (FOV) 90° at $V_b \leq 3$ V and for T $\leq$ 100 K, which is believed to be the highest BLIP temperature ever observed in a QWIP. The ultra-low dark current observed in this PSL-QWIP can be attributed to the following factors: (i) The dark current is dominated by the thermionic emission from the ground light-hole state (E_{LH1}) and transports through the heavy-hole continuum states E_{HH3} above the barrier. The thermionic emission current is greatly reduced due to the increase of the effective barrier height (i.e., E_b = 155 meV) by the tensile strain created in the quantum well, (ii) since the bandwidth of heavy-hole continuum states E_{HH3} is very narrow ($\sim$ 10 meV, compared to 25 meV for the unstrained p-type QWIP), a reduction of dark current by about ten times is expected, (iii) due to the large heavy-hole effective mass and the short heavy-hole lifetime in the E_{HH3} continuum states (i.e., lower optical gain; about ten times smaller than that of n-type QWIPs), the dark current can be further reduced, and (iv) a lower thermally generated hole density p_o can also lower the dark current. From the above analysis, the dark current in the PSL-QWIP are expected to reduce by several orders of magnitude over the unstrained p-type and n-type QWIPs, as is clearly shown in Fig. 3.1.3.

The responsivity of the detector under normal incidence illumination was measured as a func-

tion of temperature, bias voltage, and wavelength using a globar and automatic PC-controlled single-grating monochrometer system. The measured photocurrents versus wavelength for both positive and negative biases are shown in Figs. 3.1.4a and 3.1.4b, respectively, at λ_p = 8.1 μm and T = 77 K. The peak response wavelength was found to be at λ_p = 8.1 μm, which corresponds to the intersubband transition between the confined ground light-hole state (E_{LH1}) and the continuum heavy-hole states (E_{HH3}), as is illustrated in Fig. 3.1.1. The cutoff wavelength for this QWIP was found to be λ_c = 8.8 μm with a spectral bandwidth of $\Delta\lambda/\lambda_p$ = 12%. Since two other heavy-hole bound excited states are confined inside the quantum wells with very low tunneling probability off the thicker barrier layer, no photoresponse from these two heavy-hole states was detected. Responsivities of 34 mA/W at V_b = 4 V and 51 mA/W at V_b = - 4 V were obtained for this PSL-QWIP at 77 K. The maximum BLIP detectivity, D^*_{BLIP}, at λ_p = 8.1 μm was found to be 5.9×10^{10} cm-Hz$^{1/2}$/W (with a responsivity, R_A = 18 mA/W) at V_b = 2 V, FOV = 90° and T = 77 K. The quantum efficiency for our PSL-QWIP was estimated to be $\sim$ 50 % from the responsivity measurement, assuming a photoconductive gain of g = 0.015.

In a BLIP QWIP, the dominant noise source is due to the photon noise while all other noise sources are negligible in comparison. The photon noise is calculated based on the arrival statistics of the incoherent photons. The background photon noise current i_{np} is given by[15,16]

$$i^2_{np} = 4e^2\eta g^2(P_b/2)B/(h\nu), \tag{20}$$

where P_b is the incident background optical power, B is the QWIP bandwidth, η is the absorption quantum efficiency, ν is the incident photon frequency, and g is the photoconductive gain. The optical photosignal current I_p can be approximated by

$$I_p = (e/h\nu)\eta g(P_s/2), \tag{21}$$

where P_s is the incident optical signal power. The factor of 1/2 inside the parenthesis of P_b and P_s given in the above two equations is due to the incident optical polarization selectivity for n-type QWIPs (without 1/2 for p-type QWIPs). By setting the signal-to-noise power ratio equal to unity, the background-limited noise equivalent power $(NEP)_{BLIP}$ and detectivity D^*_{BLIP} for n-type QWIPs can be expressed by

$$(NEP)_{BLIP} = 2\sqrt{2h\nu BP_b/\eta}, \tag{22}$$

$$D^*_{BLIP} = \sqrt{AB}/(NEP)_{BLIP} = (1/2)\frac{\lambda_p}{\sqrt{2}hc}\left(\frac{\eta}{Q_b}\right)^{1/2}, \tag{23}$$

where A is the active area of the detector, and $Q_b = P_b/(A\ h\nu)$ is the incident photon flux from the background for a given spectral bandwidth $\Delta\nu$ and a peak wavelength λ_p. Q_b is given by

$$Q_b = \frac{2\pi}{c^2}\frac{\nu^2\Delta\nu}{e^{h\nu/KT}-1}\sin^2\left(\frac{\theta}{2}\right), \tag{24}$$

where θ is the field of view (FOV). It is noted that Eq.(11) for the detectivity expression should be multiplied by a factor of $\sqrt{2}$ to account for the absorption of both optical polarizations of the IR radiation in p-type QWIPs.

For a non-BLIP QWIP, since the electronic noise from the detector is no longer negligible, the term Q_b should be replaced by $(Q_b + Q_d)$, where Q_d is the equivalent photon flux which generates the same level of the electronic noise. Thus, the detectivity can be calculated by

$$D^* = \frac{\lambda_p}{2hc}\frac{\eta\sqrt{g}}{\sqrt{J_d/e}} \tag{25}$$

where J_d is the dark current density. It is noted that the detectivity D^* for a non-BLIP detector depends photoconductive gain g while the detectivity for the BLIP is independent of g.

The responsivity for the PSL-QWIP was calibrated by using a standard pyroelectric detector and lock-in amplifier technique. Asymmetric responsivities of 34 mA/W at bias + 4 V and 51 mA/W at bias - 4 V were obtained. The maximum BLIP detectivity D^*_{BLIP} at λ_p = 8.1 μm was calculated to be 5.9×10^{10} cm $Hz^{1/2}/W$ with a responsivity R_A = 18 mA/W at bias + 2 V, FOV = 90° and T = 77 K. The quantum efficiency for the PSL-QWIP was estimated from the responsivity measurement and a reasonable photoconductive gain g = 0.015 was used in the BLIP detectivity calculation. When the Johnson noise and the readout noise are ignored, the %BLIP for positive and negative bias are evaluated by using

$$\%BLIP \approx \frac{i_{np}}{(i_{np}^2 + i_{nd}^2)^{1/2}} \tag{26}$$

where $i_{np,nd}$ are the 300 K background photocurrent noise and dark current noise, respectively. Figure 3.1.5 shows the calculated %BLIP for the positive and negative biases. A nearly full BLIP detection was achieved at bias voltages less than |2| V. As a result of the fully BLIP detection in our PSI-QWIP, the noise equivalent temperature difference (NEΔT) is expected to improved significantly for the focal plane array thermal imaging applications.

In conclusion, we have demonstrated for the first time a new utra-low dark current, normal incidence p-type strained-layer *InGaAs/InAlAs QWIP with BLIP for* $V_b \leq 3$ *V and* $T \leq 100$ *K*. The BLIP detectivity for this PSL-QWIP was greatly enhanced by the biaxial tensile strain introduced

in the wells leading to the inversion of heavy-hole and light-hole ground state in the well. By further optimizing the quantum well dopant density, strength of the biaxial tensile strain, and structure parameters, it is anticipated that a high performance PSL-QWIP can be fabricated for large area infrared focal plane arrays image sensor systems with BLIP for T$\leq$ 100 K.

References

1. B. F. Levine, J. Appl. Phys. 74(8), R1-R-81, Oct.15, 1993.
2. B. F. Levine, R. J. Malik, J. Walker, K. K. Choi, C. G. Bethea, D. A. Kleinman, and J. M. Vandenberg, Appl. Phys. Lett. **50**, 273 (1987).
3. L. S. Yu, **S. S. Li**, Appl. Phys. Lett. **59**, 1332 (1991).
4. G. Hasnain, B. F. Levine, C. G. Bethea, R. A. Logan, J. Walker, and R. J. Malik, Appl. Phys. Lett. **54**, 2515 (1989).
5. J. Y. Andersson and L. Lundqvist, J. Appl. Phys. **71**, 3600 (1992).
6. B. F. Levine, S. D. Gunapala. J. M. Kuo, S. S. Pei, and S. Hui, Appl. Phys. Lett. **59**, 1864 (1991).
7. J. Katz, Y. Zhang, and W. I . Wang, Electron. Lett. **28**, 932 (1992).
8. W. S. Hobson, A. Zussman, B. F. Levine, and J. deJong, J. Appl. Phys. **71**, 3642 (1992).
9. J. W. Matthews and A. E. Blakeslee, J. Cryst. Growth **32**, 265 (1976).
10. Landolt-B(o)rnstein, Numerical Data and Functional Relationships in Science and Technology, O. Madelung, ed., Group III, **17a, 22a**, Springer-Verlag, Berlin (1986).
11. G. Ji, D. Huanf, U. K. Reddy, T. S. Henderson, R. Houre, and H. Morkoç, J. Appl. Phys. **62**, 3366 (1987).
12. T. P. Pearsall, Semiconductors and Semimetals, **32**, 55 (1990).
13. H. Asai, and Y. Kawamura, Appl. Phys. Lett. **56**, 746 (1990).
14. H. Xie, J. Katz, and W. I. Wang, Appl. Phys. Lett. **59**, 3601 (1991).
15. R. T. Kuroda and E. Garmire, Infrared Phys. **34**, 153 (1993).
16. L. R. Ram-Mohan, K. H. Yoo, and R. L. Aggarwal, Phys. Rev B **38**, 6151 (1988).
17. J. M. Luttinger and W. Kohn, Phys. Rev. **97**, 869 (1956).
18. J. M. Luttinger, Phys. Rev. **102**, 1030 (1956).
19. G. L. Bir and G. E. Pikus, Symmetry and Strain-Induced effects in Semiconductors, Wiley, New York (1974).
20. E. L. Derniak and D. G. Crowe, Optical Radiation Detectors, Wiley, New York (1984).
21. H. C. Liu, Z. R. Wasilewski, and M. Buchanan, Appl. Phys. Lett., **63**, 761 (1993).

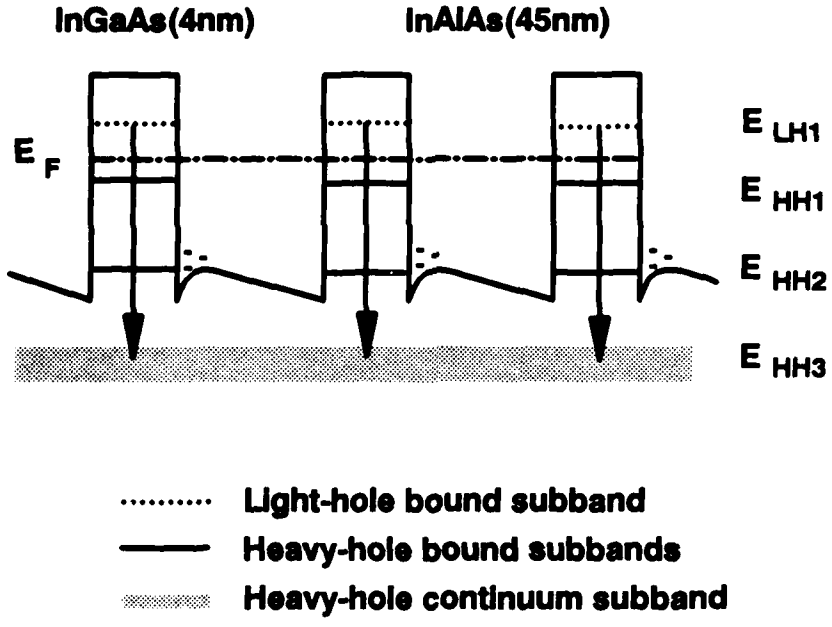

Fig.3.1.1 The energy band diagram for a p-type strained-layer (PSL) InGaAs/InAlAs QWIP showing the energy band bending due to doping impurity migration effect.

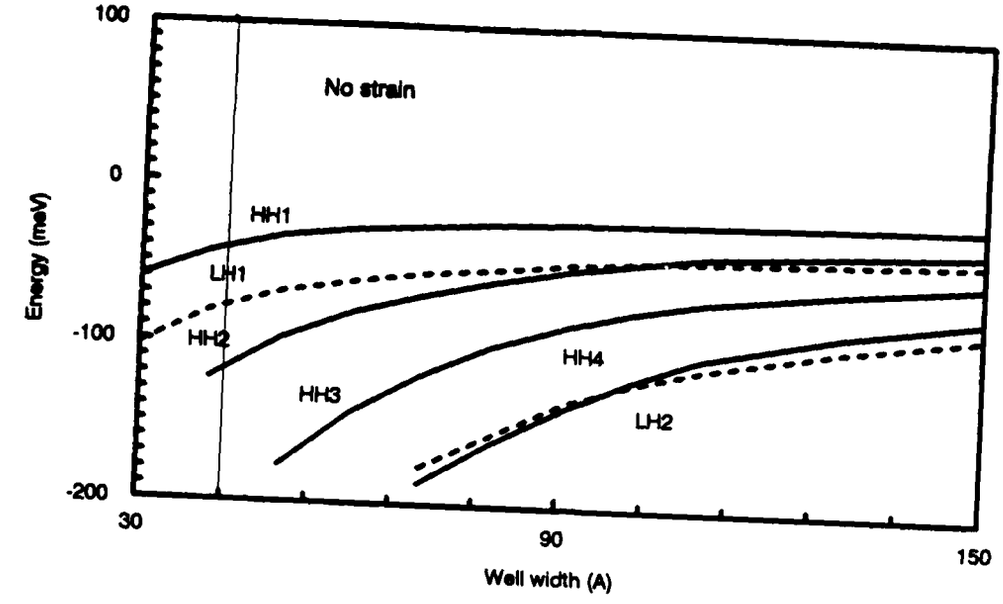

(a)

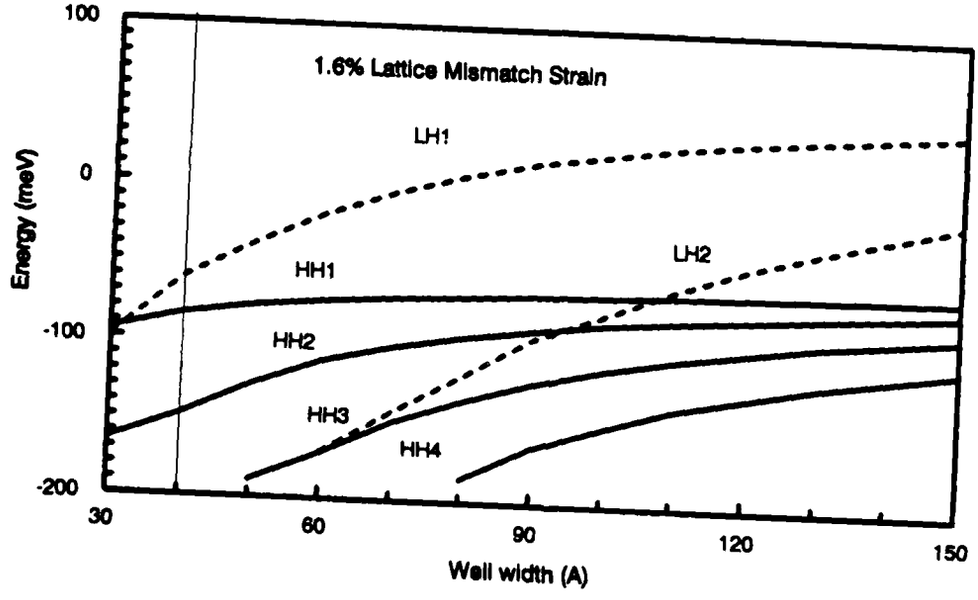

(b)

Fig.3.1.2 The energy band structures at the valence band zone-center for a p-type InGaAs/InAlAs QWIP as a function of well thickness (a) without and (b) with biaxial tensile strain in quantum well.

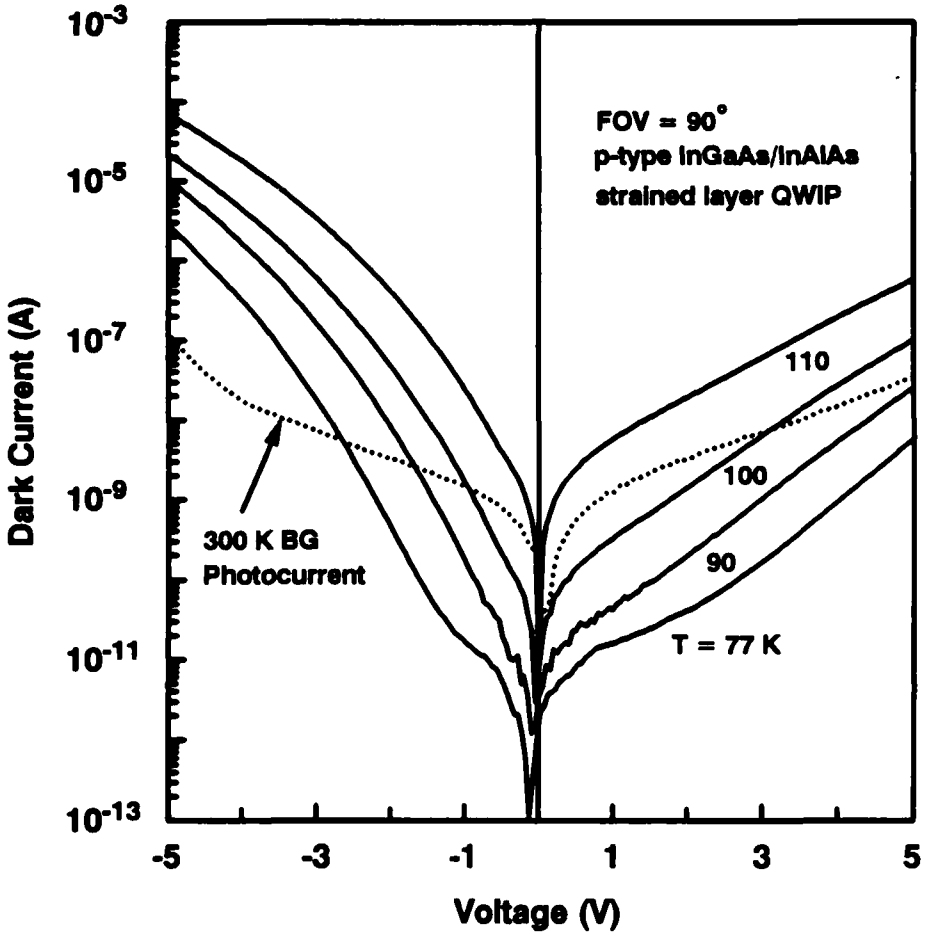

Fig.3.1.3 The dark current and 300 K background photocurrent as a function of bias voltage for the InGaAs/InAlAs PSL-QWIP for 77 < T < 110 K and FOV = 90 °.

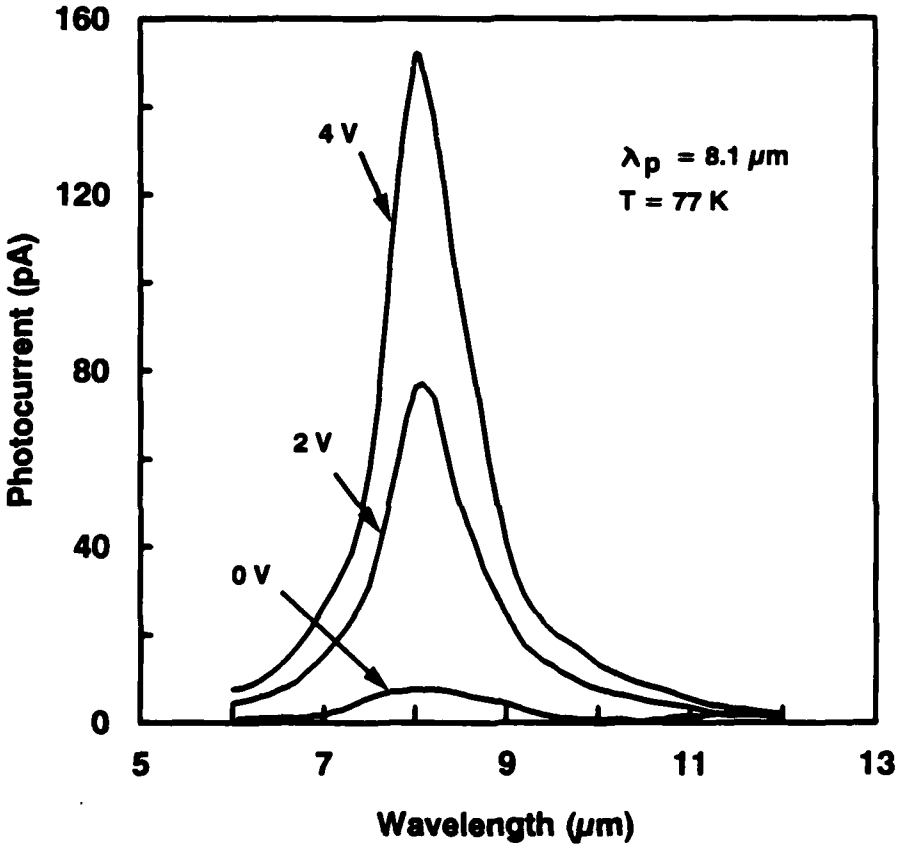

Fig.3.1.4a The photocurrent versus wavelength for the InGaAs/InAlAs PSL-QWIP measured at different positive bias voltages and 77 K.

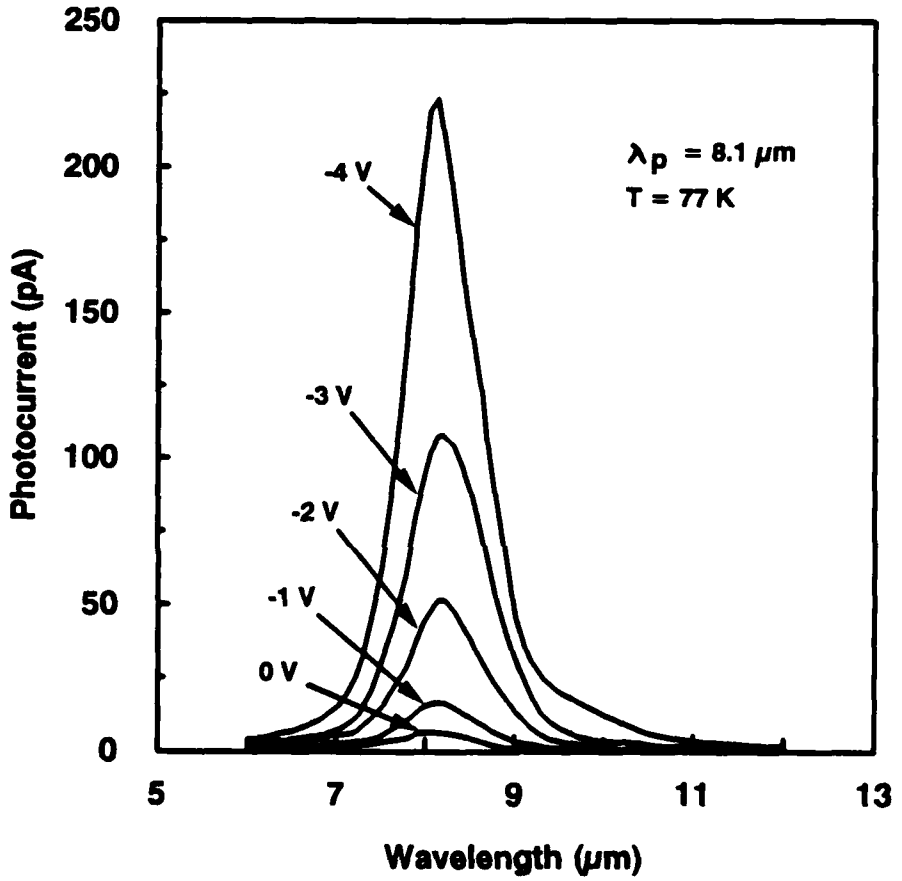

Fig.3.1.4b The photocurrent versus wavelength for the InGaAs/InAlAs PSL-QWIP measured at different negative bias voltages and 77 K.

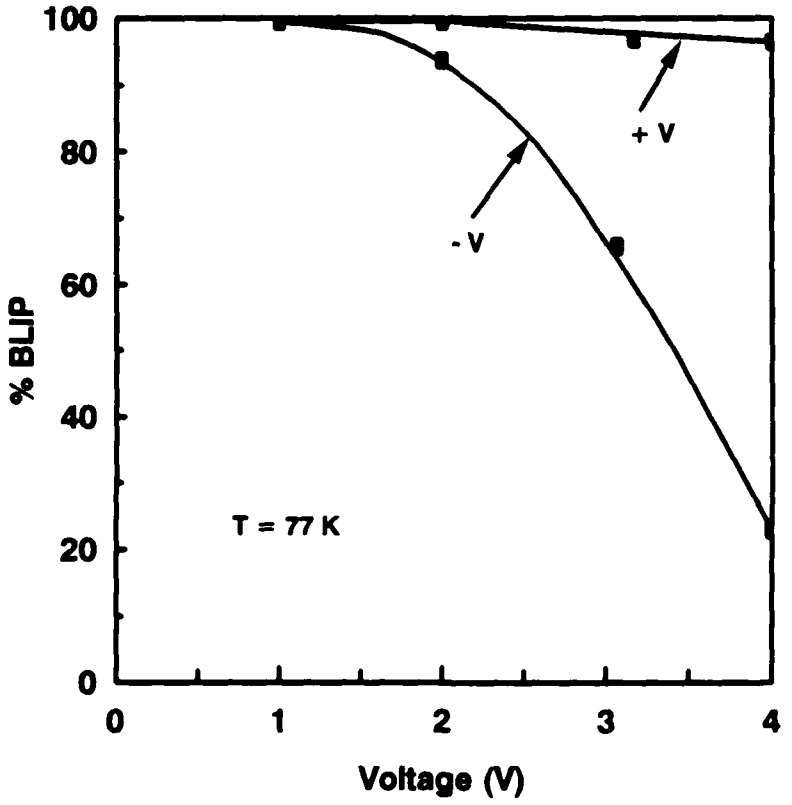

Fig.3.1.5 % BLIP of the InGaAs/InAlAs PSL-QWIP versus voltage at different positive and negative bias voltages and 77 K.

3.2 Design of A 2-D Circular Mesh Metal Grating Coupler for QWIPs

Summary: Numerical analysis of a two-dimensional (2-D) circular mesh metal grating coupler for a GaAs based quantum well infrared photodetector (QWIP) has been carried out. The coupling efficiency of such a planar metal grating is calculated as a function of normalized wavelength $s = \lambda/g$ and normalized aperture radius $h = a/g$, where 'g' is the grating period and 'a' is the aperture radius. The universal plots displaying the normalized total power and absorption angle of the higher-order diffracted waves versus normalized wavelength provide a convenient way for designing the optimum grating coupler for the GaAs QWIPs. The results showed a 2.7 times enhancement of photo-responsivity for such a grating coupler over the 45° edge illuminated QWIP.

3.2.I Introduction

In our previous work we have reported the design of 2-D square dot reflection metal grating and 2-D square mesh metal grating couplers for n-type QWIPs[1,2]. In this section, we present the theoretical and experimental study of a planar 2-D circular mesh metal grating coupler formed on a GaAs QWIP. The results showed that back illumination performs better than that of front illumination for the circular mesh metal grating coupled QWIP. In the following, we consider the electromagnetic (EM) waves impinging on a 2-D circular mesh metal grating coupled QWIP under normal incident back illumination.

Light coupling is polarization independent provided that the individual unit cell and cell arrangement of the grating are of highly symmetry. For the circular aperture mesh metal grating both square symmetry (Fig. 3.2.1(a)) and hexagonal symmetry (Fig. 3.2.1(b)) structures possess the highest possible symmetry, and are polarization independent. It has been shown that only the TM components of the grating diffracted waves lead to intersubband transition in the quantum wells. Besides, the quantum efficiency of a QWIP is a function of the total power and absorption angle of the higher-order TM diffracted waves. In the 2-D circular aperture metal grating shown in Fig.3.2.1, under normal incident illumination, the normalized total power of each order diffracted waves depends on the 'normalized wavelength' $s = \lambda/g$ and the 'normalized aperture radius' $h = a/g$ (where g is the grating period and λ is the free space wavelength, and a is the radius of the circular aperture in the metal grating). Furthermore, the absorption angle used in determining the absorption constant depends on the parameter s and the order of diffraction. Based on this analysis, several universal charts of total power and absorption angle of higher-order TM diffracted waves are presented below to provide a convenient designing tools for the 2-D circular

aperture mesh metal grating coupled GaAs QWIPs.

3.2.2 Basic Formulation

According to the diffraction properties of grating, the unknown scattered waves on both side of the grating can be expanded into a complete set of Floquet modes $\vec{\Phi}_{pqr}$, with two spatial harmonic number p and q, and a third subscript r used to denote TE or TM modes. The unit power density EM wave is normally incident on the perfect conducting grating of infinitesimal thickness as shown in Fig.3.2.1(c). The vector orthonormal mode functions for the TE and TM Floquet modes transverse with respect to $\hat{z}$ can be expressed by

$$\vec{\Phi}_{pq1} = G(\sin\phi_{pq}\hat{x} - \cos\phi_{pq}\hat{y})e^{-j(k_x^p x + k_y^{pq} y)} \qquad \text{for TE modes}$$

$$\vec{\Phi}_{pq2} = G(\cos\phi_{pq}\hat{x} + \sin\phi_{pq}\hat{y})e^{-j(k_x^p x + k_y^{pq} y)} \qquad \text{for TM modes} \tag{27}$$

where the normalized factor G is written in terms of grating period g

$$\begin{aligned} G &= \frac{1}{g} && \text{for square symmetry} \\ &= \sqrt{\frac{2}{\sqrt{3}}}\frac{1}{g} && \text{for hexagonal symmetry} \end{aligned} \tag{28}$$

the time dependence $e^{j\omega t}$ is omitted, and the wave vectors k_x^p and k_y^q in the x and y axes are given respectively by

$$\begin{aligned} k_x^p &= \frac{2\pi}{g}p = k\sin\theta_{pq}\cos\phi_{pq} \\ k_y^{pq} &= \frac{2\pi}{g}q = k\sin\theta_{pq}\sin\phi_{pq} && \text{for square symmetry} \\ &= \frac{2\pi}{\sqrt{3}g}(2q-p) = k\sin\theta_{pq}\sin\phi_{pq} && \text{for hexagonal symmetry} \end{aligned} \tag{29}$$

where θ_{pq} and ϕ_{pq} are the corresponding spherical coordinates for the wave propagating vector $\vec{k}$ of (p,q) order Floquet mode, and $p,q = 0,\pm1,\pm2,\ldots,\pm\infty$. The z direction wave vector k_z^{pq} depends on p and q, which is real for propagating modes, pure imaginary for evanescent modes. Assuming that the impedances looking into the quantum well region from $z = 0^-$ plane are equal to that of bulk GaAs, the modal impedances η_{pqr}^d and η_{pqr} on both sides of the metal grating for the TE and TM waves can be easily derived. The boundary condition needs the tangential electric field vectors to be continuous within the circular aperture located at $z = 0$, that is

$$\sum_{r=1}^{2} A_{00r}\vec{\Phi}_{00r} + \sum_{p,q}\sum_{r=1}^{2} R_{pqr}\vec{\Phi}_{pqr} = \sum_{p,q}\sum_{r=1}^{2} T_{pqr}\vec{\Phi}_{pqr} \qquad \text{within the aperture} \tag{30}$$

where the first summation on the left-hand side is the expansion of the incident wave with a unit power density, the second summation on the left-hand side is the expansion of the reflected waves, the summation on the right-hand side is the expansion of the transmitted waves, A_{00r} is the magnitude of incident field component which depends on the polarization direction, R_{pqr} and T_{pqr} is the reflection coefficient and transmission coefficient of the Floquet mode, respectively.

The orthonormal waveguide modes $\vec{\Pi}_{mnl}$ that satisfy the aperture boundary condition of the circular aperture itself other than the Floquet modes $\vec{\Phi}_{pqr}$ are selected as the second set of linear independent basis to represent the unknown electric field distribution in the aperture. As a result, the transverse electric field vector is written as $\sum_{p,q}\sum_{r} T_{pqr}\vec{\Phi}_{pqr} = \sum_{mn}\sum_{l} W_{mnl}\vec{\Pi}_{mnl}$, where

$$\vec{\Pi}_{mn1}(\rho,\psi) = \sqrt{\frac{2-\delta_{0n}}{\pi}}\frac{1}{J_m(x'_{mn})\sqrt{(x'_{mn})^2-m^2}}\frac{x'_{mn}}{a} \left[\hat{\rho}\frac{m}{\frac{x'_{mn}}{a}\rho}J_m\left(\frac{x'_{mn}}{a}\rho\right)\left\{\begin{array}{c}\sin m\psi\\ -\cos m\psi\end{array}\right\} + \hat{\psi}J'_m\left(\frac{x'_{mn}}{a}\rho\right)\left\{\begin{array}{c}\cos m\psi\\ \sin m\psi\end{array}\right\}\right] \quad (31)$$

and

$$\vec{\Pi}_{mn2}(\rho,\psi) = \sqrt{\frac{2-\delta_{0n}}{\pi}}\frac{1}{aJ_{m-1}(x_{mn})} \left[\hat{\rho}J'_m\left(\frac{x_{mn}}{a}\rho\right)\left\{\begin{array}{c}\cos m\psi\\ \sin m\psi\end{array}\right\} - \hat{\psi}\frac{m}{\frac{x_{mn}}{a}\rho}J_m\left(\frac{x_{mn}}{a}\rho\right)\left\{\begin{array}{c}\sin m\psi\\ -\cos m\psi\end{array}\right\}\right] \quad (32)$$

where a is the radius of the circular aperture, (ρ,ψ,z) are the cylindrical coordinates system used, J_m is the Bessel function of the first kind with order m, x_{mn} is the nth zero of $J_m(x)$ and x'_{mn} is the nth zero of $J'_m(x)$, δ_{0n} equals 1 for $n=0$ and δ_{0n} equals 0 for $n \geq 1$. Employing method of moments, a final matrix equation can be obtained as

$$\left[Y^{MNL}_{mnl}\right][W_{mnl}] = [I_{mnl}] \quad (33)$$

where

$$Y^{MNL}_{mnl} = \sum_{p,q}\sum_{r=1}^{2}\left(\frac{1}{\eta^{d}_{pqr}} + \frac{1}{\eta_{pqr}}\right)C^{MNL*}_{pqr}C^{mnl}_{pqr}$$

$$C^{mnl}_{pqr} = \int_0^{2\pi}\int_0^{a}\vec{\Phi}^{*}_{pqr}(x,y)\cdot\vec{\Pi}_{mnl}(\rho,\phi)d\rho d\phi \quad (34)$$

both terms depend on grating geometry, W_{mnl} is the unknown coefficient, and I_{mnl} is the matrix depending on incident waves. However, it is impractical to calculate C^{mnl}_{pqr} by using numerical integral. To solve this, a hand calculated complete form of the inner product C^{mnl}_{pqr} of vector

functions is found in Appendix A. The higher-order reflection coefficients are given by

$$R_{pqr} = \sum_{mn}\sum_{l=1}^{2} W_{mnl} C_{pqr}^{mnl} \qquad p,q \neq 0,0 \tag{35}$$

The normalized power associated with (p,q)-order TM reflected wave is given by

$$\mathcal{P}_{pq2}^{refl} = \frac{|R_{pq2}|^2}{\cos\theta_{pq2}^{refl}} \tag{36}$$

Since W_{mnl} is proportional to λ^2 and C_{pqr}^{mnl} varies as $1/\lambda^2$ for a given g, the reflection coefficient R_{pqr} is a function of λ/g. Accordingly, the normalized power $\mathcal{P}_{pq2}$ is also a function of λ/g. The angle between the electric field vector of the higher-order TM reflected modes $R_{pq2}\vec{\Phi}_{pq2}$ and the $\hat{z}$ direction is defined as absorption angle γ_{pq2}, and the cosine of this angle depends on the order of diffraction and the normalized wavelength s $(= \lambda/g)$, which is given by

$$\begin{aligned} \cos\gamma_{pq2} &= \frac{s}{n_r}\sqrt{p^2+q^2} && \text{for square symmetry} \\ &= \frac{s}{n_r}\frac{2}{\sqrt{3}}\sqrt{p^2+q^2-pq} && \text{for hexagonal symmetry} \end{aligned} \tag{37}$$

where n_r is the refractive index of the detector medium, and $n_r = 3.25$ for GaAs at 77 K.

3.2.3 Results and Discussion

In the calculation, the lowest 52 waveguide modes and all the Floquet modes with $2\pi/g\sqrt{p^2+q^2} \leq 25(2\pi/\lambda)$ were included; the addition of more higher order modes made no noticeable change in the transmission and reflection coefficients. For simplicity we consider a unit power density EM wave impinging normally on the mesh metal grating, as shown in Fig.3.2.1(c). The effective coupling is due to nonzeroth-order reflected TM Floquet modes, since the TE Floquet modes have an absorption angle $\gamma = 90°$ and the evanescent mode produce no photo-signal in intersubband absorption. In order to develop the universal relationship of the 2-D circular aperture metal grating coupler, the grating parameters are normalized to grating period g, that is, normalized wavelength '$s = \lambda/g$' and normalized aperture radius '$h = a/g$' to facilitate illustration.

A. Circular Mesh Grating with Square Symmetry

Figure 3.2.2 illustrates a universal plot, which shows the normalized total power of the first-order TM diffracted waves $R_{012}\vec{\Phi}_{012}$, $R_{0-12}\vec{\Phi}_{0-12}$, $R_{-102}\vec{\Phi}_{-102}$ and $R_{102}\vec{\Phi}_{102}$ as a function of s for different values of h. The first-order diffracted waves emerge when the wavelength of the IR radiation in GaAs is smaller than the grating period, that is, $s = \lambda/g < 3.25$. For the same reason,

within the spectral range shown in Fig.3.2.2, only zeroth-order far field transmitted waves $T_{00i}\vec{\Phi}_{00i}$ ($i = 1,2$) in the free space might be found, and all other higher-order transmitted waves were evanescent modes. This is due to the fact that free space wavelength λ is much greater than the grating period g. In addition, the square symmetry arrangement of the grating is indistinguishable between x and y directions. The total normalized power of the first order diffracted waves generated by x and y components of the incident waves remain the same for different incident polarizations. In other words, the coupling of the grating is polarization independent. Figure 3.2.3 illustrates the normalized total power of the second-order TM diffracted components $R_{\pm 112}\vec{\Phi}_{\pm 112}$ and $R_{\pm 1-12}\vec{\Phi}_{\pm 1-12}$ as a function of s for different values of h. A comparison of Figs.3.2.2 and 3.2.3 reveals that the grating which excites larger power of the first-order diffracted waves will prohibit the power of the second-order diffracted waves. The second-order diffracted waves emerge for $s < 2.298$ with a total power about 50 % smaller than that of the first-order diffracted waves.

During grating fabrication process, it is noted that the grating period g remains constant, while the aperture radius may be varied. Under this process consideration, a figure relates the total power of the first-order diffracted waves to $h = a/g$ within the most effective coupling regime $2.8 \leq s \leq 3.2$ is plotted in Fig.3.2.4. It is shown that $a/g = 0.36$ is the ratio of aperture radius which not only is insensitive to the variation in aperture radius but also maximizes the normalized diffracted power $\mathcal{P}_{eff}$. This implies that $a/g = 0.36$ is the optimum aperture radius for the square symmetry circular aperture metal grating.

B. Circular Mesh Grating with Hexagonal Symmetry

Figure 3.2.5 shows the universal plot illustrating the normalized total power of the first-order TM diffracted waves $R_{\pm 102}\vec{\Phi}^{TM}_{\pm 10}$, $R_{0\pm 12}\vec{\Phi}^{TM}_{0\pm 1}$ and $R_{\pm 1\pm 12}\vec{\Phi}^{TM}_{\pm 1\pm 1}$ as a function of s for different values of h. The first-order diffracted waves emerge when the wavelength of the IR radiation in GaAs is smaller than $\sqrt{3}/2g$. The second-order TM diffracted waves consist of $R_{\mp 1\pm 12}\vec{\Phi}^{TM}_{\mp 1\pm 1}$, $R_{\pm 1\pm 22}\vec{\Phi}^{TM}_{\pm 1\pm 2}$, and $R_{\pm 212}\vec{\Phi}^{TM}_{\pm 21}$, which exist only for $s < 2.298$ with a total power about one tenth of that of the first-order diffracted waves. Of course, the total normalized power of each order diffracted waves is independent of the incident polarization. Again, the figure relates the total power of the first-order diffracted waves to h within the most effective coupling regime $2.4 \leq s \leq 2.8$ is plotted in Fig.3.2.6. It is shown that $a/g = 0.31$ is the optimum normalized radius for the hexagonal symmetry circular aperture metal grating.

By comparing Figs.3.2.2 and 3.2.5, it is seen that a maximum coupling efficiency for the square

symmetry circular aperture grating is about 1.08 times larger than that of hexagonal symmetry grating coupler. On the other hand, the latter has a 1.44 times wider available bandwidth (the band between the normalized wavelength at which the 1st and 2nd diffracted waves begin to propagate) than that of the former.

The circular aperture mesh metal grating coupler used in our experiment is the square symmetry one discussed above. For effective coupling, the period of mesh metal grating is selected in the region where s falls between 2.298 and 3.25 by using the first-order TM diffracted waves. Within this region, the $\cos^2\gamma$ is greater than 1/2, which is corresponding to that of a 45° angle light launching. The grating parameters are $g = 3.3\mu$m, $a = 1\mu$m, or $a/g = 0.6$ with the grating coupling characteristic curve shown in Fig.3.2.7, which is obtained by multiplying the grating period $g = 3.3\mu$m to the coordinate of curve $a/g = 0.6$ in Fig.3.2.2. The cut-off wavelength of the grating is 10.725μm. The grating coupled GaAs QWIP used in the present analysis is composed of 20-period GaAs multiquantum wells with a well width of $40\mathring{A}$ and a dopant density 1.2×10^{18} cm^{-3} and an $Al_{0.25}Ga_{0.75}As$ barrier thickness of $480\mathring{A}$. In this QWIP, the 2-D electrons in the continuous band can move freely in the direction perpendicular to the quantum well layers, which in turn produce an electric current through the QWIP.

The responsivity R_I for the QWIP can be calculated by

$$R_I = \left[\mathcal{P}_{eff}(1 - e^{-\alpha \cdot l})\right] g_o \frac{\lambda}{1.24} \tag{38}$$

where $\mathcal{P}_{eff}$ is the effective coupling power of the IR radiation, and l is the total length of the doped quantum wells, and the terms in the square brackets is the expression of quantum efficiency η. In the present case, $\mathcal{P}_{eff}$ is the normalized total power of the first order diffracted waves, and $l = (40\mathring{A}/\text{period}) \cdot (20 \text{ periods}) = 800\mathring{A}$. The optical gain g_o is estimated by the measured results of a 45° angle edge detector at bias $V_b = -1V$. The intersubband absorption constant is given by

$$\alpha = |M|^2 F \cos^2\gamma \tag{39}$$

where γ is the absorption angle given in Eq.(11) or Fig.3.2.7. F is a function of wavelength λ and the parameters of a specific quantum well structure; M is the envelop matrix element, and a 60% continuous band split is assumed. A comparison between the theoretical calculation and the experimental data of responsivity is illustrated in Fig.3.2.8. As shown in this figure, the solid line represents the theoretical responsivity of the grating with parameters $g = 3.3\mu$m and $a = 1\mu$m, which results in a 2.7 times enhancement over that of 45° edge detector. The responsivity of the

grating with parameters $g = 4\mu m$ and $a = 1.1\mu m$ is also illustrated in Fig.3.2.8, which shows that the grating having normalized wavelength $2.298 \leq s \leq 3.25$ is a more effective grating coupler. Furthermore, by choosing a grating of $g = 3.3\mu m$, $a = 1.2\mu m$, i.e. $a/g = 0.36$, a greater responsivity enhancement can be obtained.

In conclusion, we have performed a detailed analysis and numerical calculations of a 2-D circular aperture mesh metal grating coupled GaAs QWIP. It is shown that for a given QWIP material, the total power and the diffracted angle of the higher-order TM diffracted waves depend on two normalized parameters $s = \lambda/g$ and $h = a/g$, which are functions of wavelength and grating dimension. The optimum grating period and aperture radius can be obtained for any specific infrared spectrum by scaling the universal curves shown in Fig.3.2.2 and Fig.3.2.4. Moreover, the responsivity for a 2-D metal grating coupled QWIP can be calculated from these universal plots.

References

1. B. F. Levine, S. D. Gunapala, and M. Hong, Appl. Phys. Lett. **59**, 1969 (1991).
2. K. M. S. V. Bandara, D. D. Coon, and Byungsung O, Appl. Phys. Lett. **53**, 1931 (1988).
3. S. D. Gunapala, B. F. Levine, and Naresh Chand, J. Appl. Phys. **70**, 385 (1991).
4. E. Rosencher, E. Martinet, F. Luc. Ph. Bois, and E. Böckenhoff, Appl. Phys. Lett. **59**, 3255 (1991).
5. K. K. Choi, L. Fotiadis, M. Taysing-Lara, and W. Chang, Appl. Phys. Lett. **59** 3303 (1991).
6. B. F. Levine, C. G. Bethea, G. Hasnain, V. O. Shen, E. Pelve, and R. R. Abbott, Appl. Phys. Lett. **56**, 851 (1990).
7. L. J. Kozlowski, G. M. William, G. J. Sullivan, C. W. Farley, R. J. Anderson, J. Chen, D. T. Cheung, W. E. Tennant, and R. E. DeWames, IEEE Trans. Electron Devices **ED-38**, 1118 (1991).
8. L. C. West and S. J. Eglash, Appl. Phys. Lett. **46**, 1156 (1985).
9. D. D. Coon and R. P. G. Karunasiri, Appl. Phys. Lett. **45**, 649 (1984).
10. M. J. Kane, M. T. Emeny, N. Apsley, C. R. Whitehouse and D. Lee, Semicond. Sci. Tech. **3**, 722 (1988).
11. B. F. Levine, K. K. Choi, C. G. Bethea, J. Walker, and R. J. Malik, Appl. Phys. Lett. **50**, 1092 (1987).
12. G. Hasnian, B. F. Levin, C. G. Bethea, R. A. Logan, J. Walker, and R. J. Malik, Appl. Phys. Lett. **54**, 2515 (1989).

13. K. W. Goossen and S. A. Lyon, Appl. Phys. Lett. **53**, 1027 (1988).

14. W. J. Li and B. D. McCombe, J. Appl. Phys. **71**, 1038 (1992).

15. J. Y. Andersson, L. Lundqvist, and Z. F. Paska, Appl. Phys. Lett. **59**, 857 (1991).

16. J. Y. Andersson and L. Lundqvist, J. Appl. Phys. **71**, 3600 (1992).

17. Y. C. Wang and **S. S. Li**, J. Appl. Phys. **74**, 2192 (1993).

18. Y.C. Wang and **S. S. Li**, accepted, J. Appl. Phys. Jan.1 issue. 1994.

19. C. C. Chen, IEEE Trans. Microwave Theory Tech. **MTT-18**, 627 (1970).

20. C. C. Chen, IEEE Trans. Microwave Theory Tech. **MTT-19**, 475 (1971).

21. N. Marcuvitz, editor, ***Waveguide Handbook***, (McGraw-Hill, New York, 1951) pp. 66.

22. R. Petit, ***Electromagnetic Theory of Gratings, Topics in Current Physics*** (Springer, Berlin, 1980) **22**, pp. 227.

23. Z. Ikonić, V. Milanović, and D. Tjapkin, Appl. Phys. Lett. **54**, 247 (1988).

24. D. Cui, Z. Chen, Y. Zhou, H. Lu, Y. Xie, and G. Yang , Infrared Phys. **32**, 53 (1991).

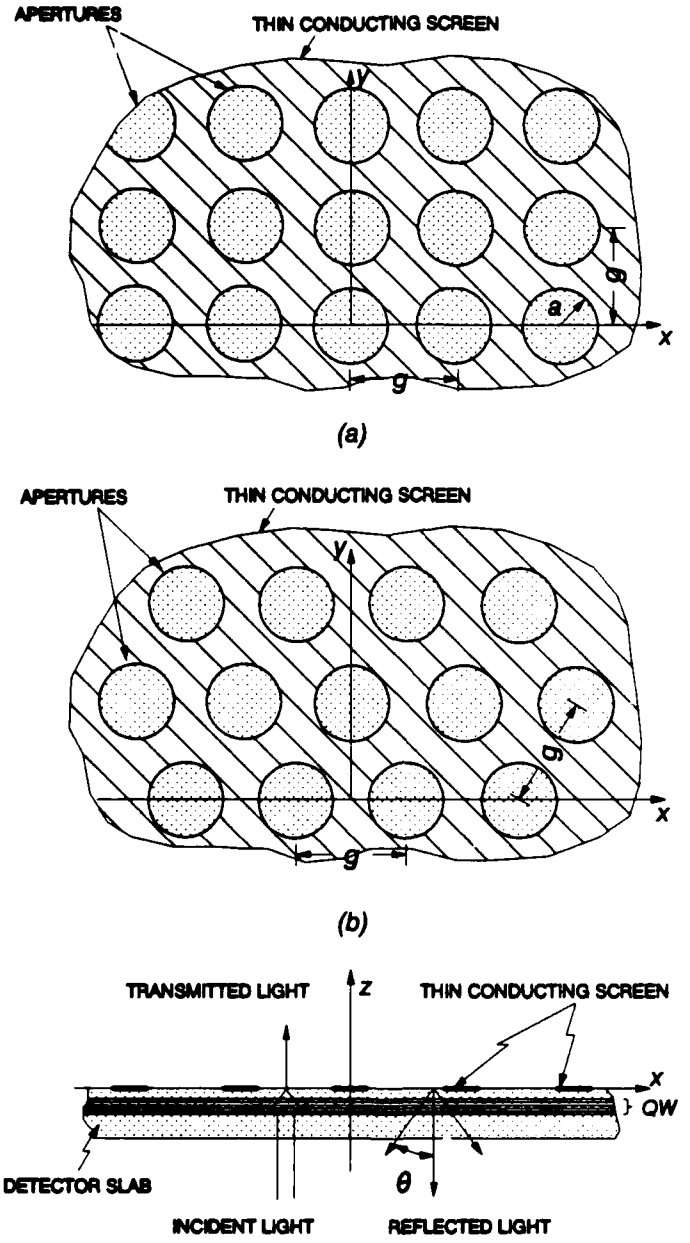

Figure 3.2.1 Top veiw of a circular mesh metal grating coupler (a) with square symmetry, (b) with a hexagonal symmetry. (c) Cross sectional view of a circular mesh metal grating with normal incident back illumination. g is the grating period and a is the radius of circular aperture.

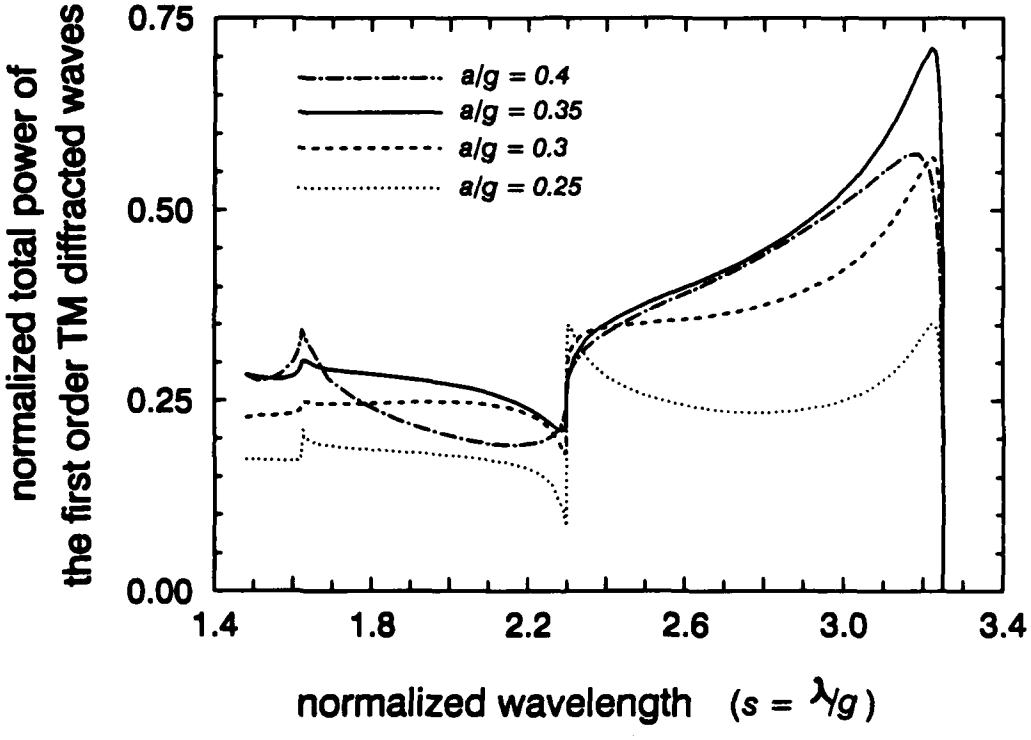

Figure 3.2.2 Normalized total power of the first-order diffracted waves versus normalized wavelength ($s = \lambda/g$) for a circular mesh metal grating coupler with square symmetry and different values of $h = a/g$.

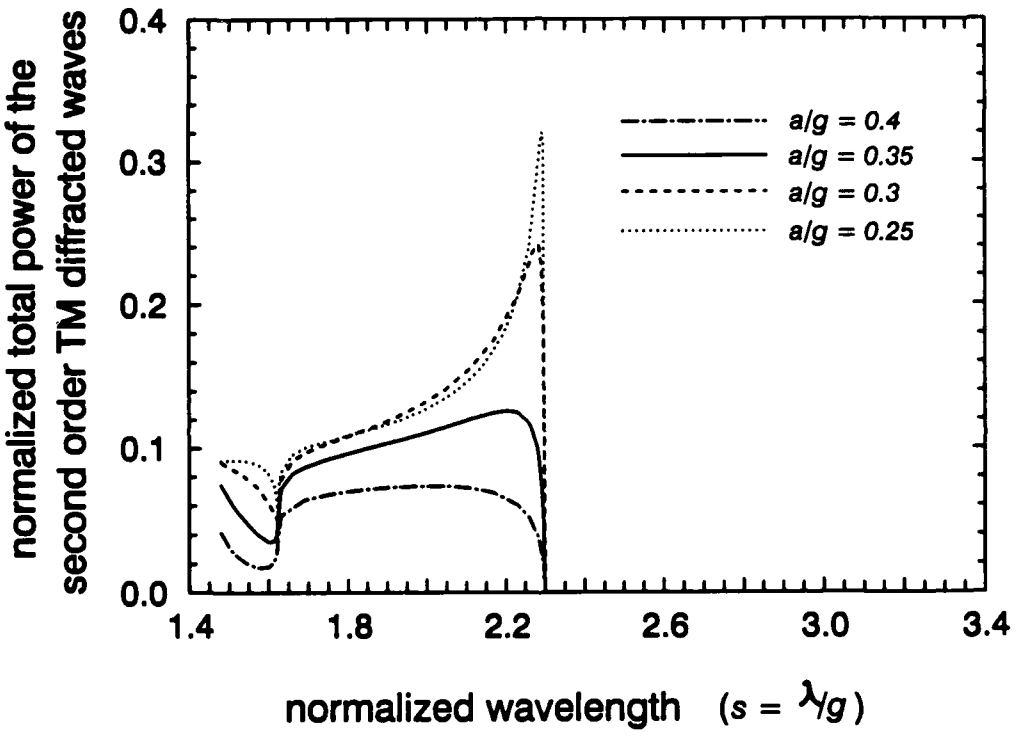

Figure 3.2.3 Normalized total power of the second-order diffracted waves versus normalized wavelength (s = λ/g) for a circular mesh metal grating coupler with square symmetry and different values of h = a/g .

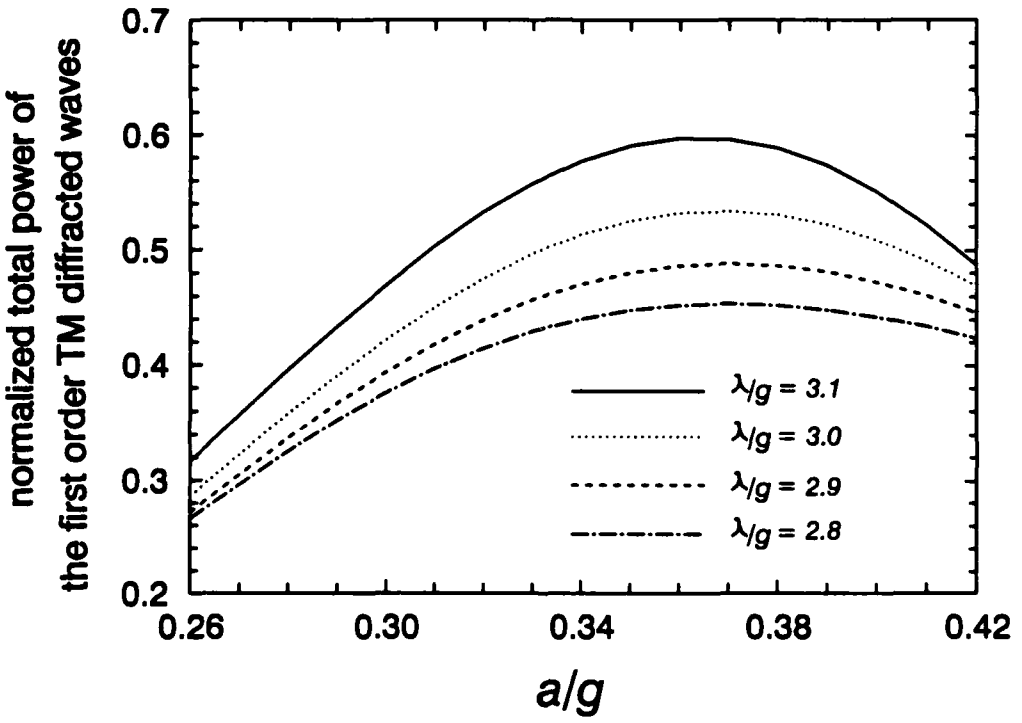

Figure 3.2.4 Normalized total power of the first-order diffracted waves versus normalized wavelength ($s = \lambda/g$) for a circular mesh metal grating coupler with square symmetry structure and different values of normalized wavelength, s.

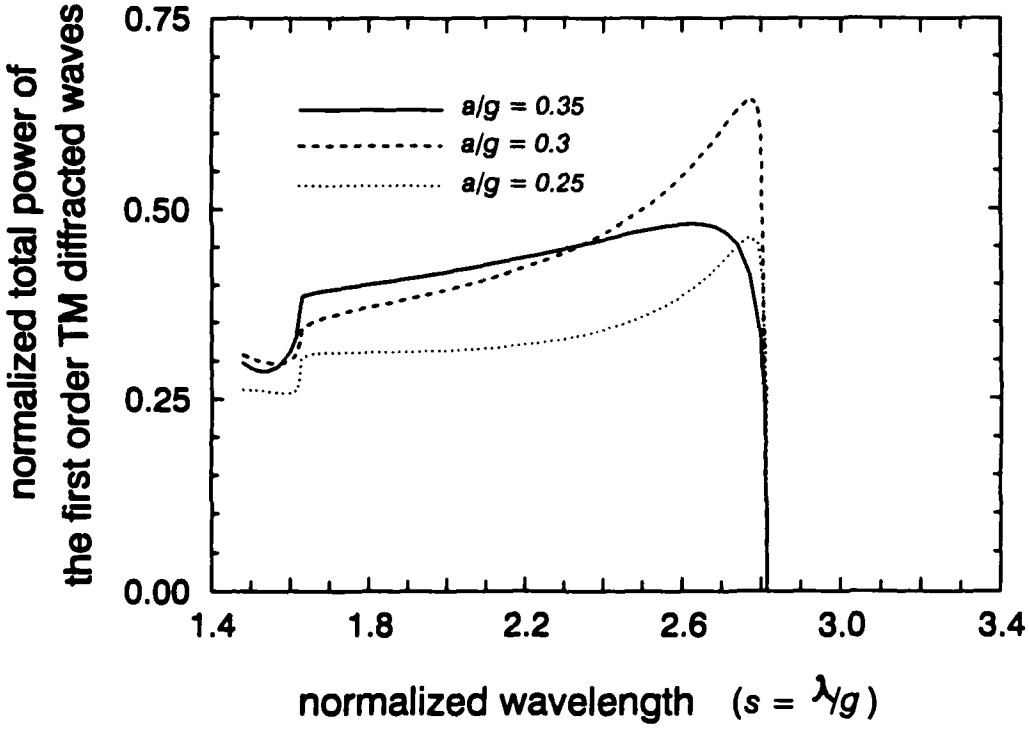

Figure 3.2.5 Normalized total power of the first-order diffracted waves versus normalized wavelength (s = λ/g) for a circular mesh metal grating coupler with hexagonal symmetry structure and different values of h = a/g.

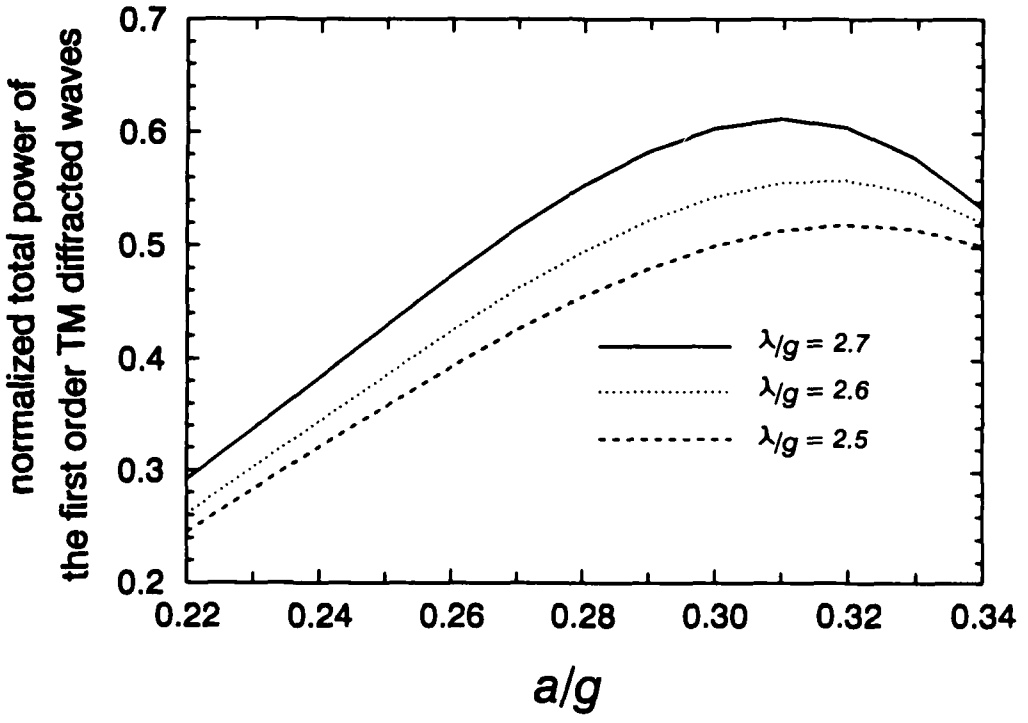

Figure 3.2.6 Normalized total power of the first-order diffracted waves versus normalized wavelength ($s = \lambda/g$) for a circular mesh metal grating coupler with hexagonal symmetry structure and different values of normalized wavelength s.

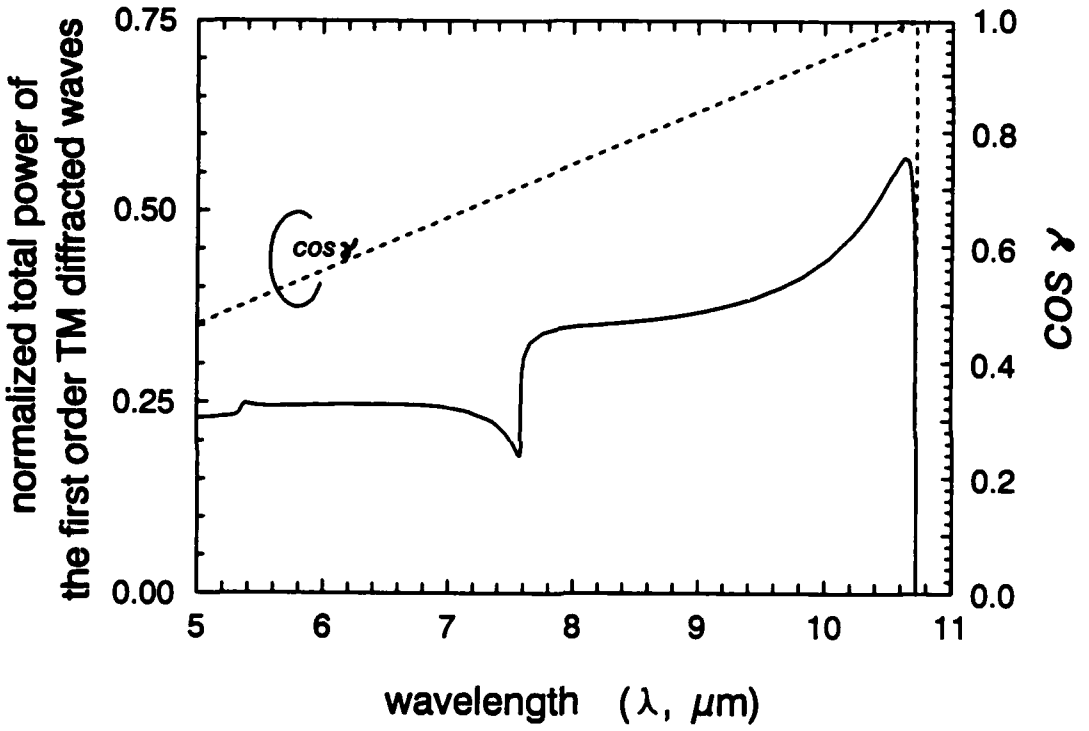

Figure 3.2.7 Normalized total power of the first-order diffracted waves and cos γ versus wavelength for a 2-D square mesh metal grating with g = 3.3 μm and a = 2 μm.

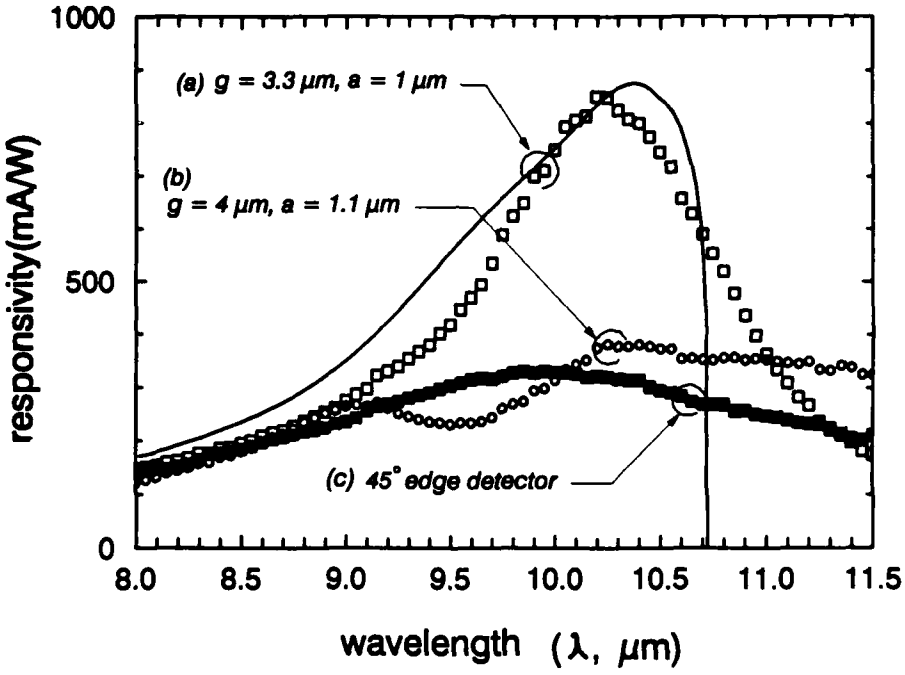

Figure 3.2.8 Spectral responsivity of a GaAs QWIP for a circular mesh metal grating coupler (a) and (b) and (a) 45 ° edge illuminated. Solid line is the calculated value for square symmetry structure. V_b = - 1 V.